

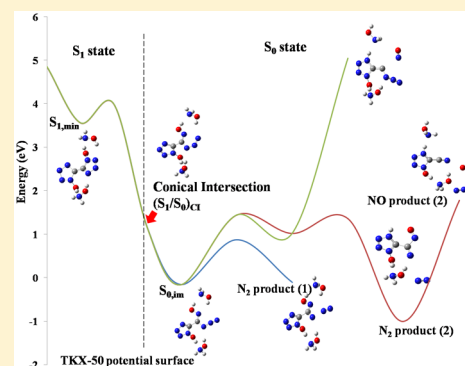
# Initial Mechanisms for the Decomposition of Electronically Excited Energetic Salts: TKX-50 and MAD-X1

Bing Yuan, Zijun Yu, and Elliot R. Bernstein\*

Department of Chemistry, Colorado State University, Fort Collins, Colorado 80523-1872, United States

## Supporting Information

**ABSTRACT:** Decomposition of energetic salts TKX-50 and MAD-X1 (dihydroxylammonium 5,5'-bistetrazole-1,1'-diolate and dihydroxylammonium 3,3'-dinitro-5,5'-bis-1,2,4-triazole-1,1'-diol, respectively), following electronic state excitation, is investigated both experimentally and theoretically. The NO and N<sub>2</sub> molecules are observed as initial decomposition products from the two materials subsequent to UV excitation. Observed NO products are rotationally cold (<25 K) and vibrationally hot (>1500 K). The vibrational temperature of the NO product from TKX-50 is (2600 ± 250) K, (1100 ± 250) K hotter than that produced from MAD-X1. Observed N<sub>2</sub> products of these two species are both rotationally cold (<30 K). Initial decomposition mechanisms for these two electronically excited salts are explored at the complete active space self-consistent field (CASSCF) level. Potential energy surface calculations at the CASSCF(8,8)/6-31G(d) level illustrate that conical intersections play an essential role in the decomposition mechanisms. Electronically excited S<sub>1</sub> molecules can nonadiabatically relax to the lower electronic state through (S<sub>1</sub>/S<sub>0</sub>)<sub>CI</sub> conical intersections. Both TKX-50 and MAD-X1 have two (S<sub>1</sub>/S<sub>0</sub>)<sub>CI</sub> conical intersections between S<sub>1</sub> and S<sub>0</sub> states, related to and leading to two different reaction paths, forming N<sub>2</sub> and NO products. N<sub>2</sub> products are released by the opening of the tetrazole or triazole rings of TKX-50 and MAD-X1. NO products are released from the amine N-oxide moiety of TKX-50, and for MAD-X1, they are produced through nitro–nitrite isomerizations. The observed rotational energy distributions for NO and N<sub>2</sub> products are consistent with the final structures of the respective transition states for each molecule on its S<sub>0</sub> potential energy surface.



## I. INTRODUCTION

Energetic materials can release large amounts of energy following external perturbations, such as sparks, shocks, heat, arcs, or photons: this energy release is sufficient to sustain detonation. In both civilian and military implementations, currently utilized highest performing explosives make use of the same strategy: cyclic and caged nitramines are employed in which the energy is derived from the oxidation of a carbon backbone by an oxidizer moiety in the same molecule (e.g., RDX, HMX, CL-20, etc.).<sup>1–4</sup> The toxicity, expensive synthesis procedures, and high sensitivities of these nitramines have, however, motivated the search for new energetic species that are safer and less expensive.<sup>1</sup>

Synthesis of safer, cheaper, and greener energetic materials with high performance and energy capacity has attracted researchers over the last decades.<sup>3</sup> Nitrogen rich heterocycles, especially nitrogen-rich azole derivatives, are the most prominent of the newer primary and secondary explosives because of their high heats of formation, high density, improved thermal stability, and low sensitivities toward external stimuli.<sup>5–9</sup> These systems have inherently many energetic N–N and C–N bonds in addition to their aromaticity and added stability of nitrogen heterocycles.<sup>5,10–12</sup> Their potential generation of nitrogen gas as an end product is highly favored for the enhancement of energy release, and avoidance of

environmental pollution and health risks.<sup>13–15</sup> In recent studies, heterocycles connected by C–C bond, such as bistriazoles and bistetrazoles, have been shown to possess the desired combination of stability, and energy storage and release properties.<sup>7,10,16,17</sup> For the triazole ring, the C=C double bond introduces a large variety of electronic states and for the tetrazole ring, a large energy content is implied.<sup>1,3,5,6,9,11,14,17–19</sup> To decrease the acidity of azole-based rings, and to balance the energetic performance and sensitivities, energetic salt materials are synthesized by varying the cations and azole-based anions for different properties.<sup>6,8–10,20,21</sup> The cations can be either nitrogen-rich bases like ammonia, hydrazine, and guanidines, or various metals, mainly alkali, alkaline earth, and transition metals.<sup>21</sup> Intra- and intermolecular hydrogen bonds can be formed in these salts which, increase material density; therefore, detonation properties, such as denotation velocity and denotation pressure, are improved as the impact and friction sensitivities of the energetic material decrease.<sup>20</sup> In addition, the low vapor pressure of energetic salts can contribute to lower toxicity and better thermal stability.<sup>20,21</sup>

Received: November 3, 2014

Revised: February 27, 2015

Published: March 5, 2015

In this study, we focus on understanding the first step in the unimolecular decomposition mechanisms for two energetic salts, dihydroxylammonium 5,5'-bistetrazole-1,1'-diolate (TKX-50) and dihydroxylammonium 3,3'-dinitro-5,5'-bis-1,2,4-triazole-1,1'-diol (MAD-X1). TKX-50 is termed a nitrogen-rich salt and dimethylammonium salt, and MAD-X1 is termed a nitrogen-rich salt and hydroxylammonium salt by the original synthesizers of these energetic materials.<sup>1,2</sup> The first decomposition step is most likely a unimolecular one: molecules comprising energetic materials are excited to high electronic energy via sparks, arcs, pressure waves, photons, etc., and they rapidly return to the ground electronic state  $S_0$  with all the acquired excitation energy now placed in the vibrational degrees of freedom of  $S_0$ , enabling rapid and energetic breaking of bonds and generation of hot small radicals and molecules. The further reactions, termed the secondary chemistry, are reactions between vibrationally hot small molecules and radicals and neighboring energetic molecules from the first decomposition step. Secondary reactions are important for energetic materials, but should not be considered as "initial steps" in the decomposition processes, which should be of a molecular origin, based on time-resolved measurements and multi-reference quantum chemical calculation.<sup>22–24</sup> The structures of TKX-50 and MAD-X1 are shown in Figure 1: comparison of

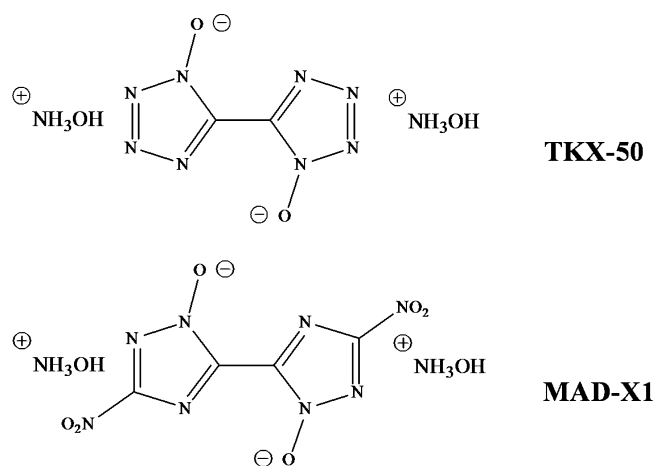


**Figure 1.** Chemical structures of TKX-50 and MAD-X1.

the energetic properties and detonation parameters of these two salts and two older energetic materials, TNT and RDX, are discussed by other researchers.<sup>1,2</sup> From refs 1 and 2, MAD-X1 has the lowest sensitivities (IS > 40 J; FS > 360 N) among these energetic materials and TKX-50 has lower impact sensitivity (IS = 20 J; FS = 120 N) than TNT (IS = 15 J; FS = 353 N) and RDX (IS = 7.5 J; FS = 120 N). Both TKX-50 and MAD-X1 have higher density, denotation pressure, and denotation velocity than TNT and RDX: these parameters for TKX-50 are better than those for MAD-X1. The energies of explosion for these two salts (TKX-50, 6025 J; MAD-X1, 5985 J) are higher than those of TNT (5258 J) and comparable to that of RDX (6190 J). As a result, the combination of good energetic performance and low sensitivity make the two energetic salts TKX-50 and MAD-X1 proper replacements for the older materials.<sup>1,2</sup> A further improvement of the energetic properties of TKX-50 and MAD-X1 accrues through introduction of the amine N-oxides, which positively influences the detonation parameters. The N–O bond of a tertiary amine

N-oxide is a relatively strong bond possessing significant double bond character, owing to  $\pi$ -backbonding by the lone electron pairs on oxygen. The formation of heterocyclic N-oxide also changes the charge distribution of the ring, which leads to an increase of the aromaticity in some cases.<sup>16</sup> Additionally, material density is increased through further possibilities to form hydrogen bonds.<sup>14,18,25</sup> TKX-50 and MAD-X1 also have a better balanced oxygen content, potentially enabling the material to oxidize all its products to their oxides, thus ensuring a maximum decomposition energy output with low heat of formation stable products, such as  $\text{CO}_2$ ,  $\text{H}_2\text{O}$ , and  $\text{N}_2$ .<sup>3,5,14,19,22,26</sup> The presence of nitro groups in MAD-X1 also contributes markedly to the oxygen balance and density.<sup>3,11</sup>

An and co-workers<sup>27</sup> studied initial steps of TKX-50 crystal thermal decomposition through density functional theory (DFT) calculations. Molecular dynamics simulations of condensed phase TKX-50 are carried out through forces from in the periodic lattice to discover the initial reaction steps at high temperature. Finite cluster DFT (B3LYP) is used to determine the reaction pathway. In their study, they found proton transfer from the  $\text{NH}_3\text{OH}$  moiety to the negative oxygen atom on the bistetrazole ring occurs at a much lower temperature than the ring breaking reaction: this proton translocation decreases the decomposition reaction barrier about 10 kcal/mol. Decomposition product  $\text{N}_2$  is released first through ring opening and fission and then  $\text{N}_2\text{O}$  is released.

Similar to our previous work,<sup>28–41</sup> we focus on the decomposition of isolated energetic materials experimentally and calculate the decomposition mechanism of single energetic molecules theoretically. These theoretical studies are of course guided by the experimentally observed results for reactions, kinetics, and dynamics in order to generate the observations and to demonstrate that current, modern ideas of organic unimolecular decomposition processes are consistent with the ultrafast behavior of energetic molecular species and their properties. The study is based on the isolated molecule behavior of energetic materials and the energy release is discussed at the single molecule decomposition level. On the basis of the phenomenon of triboluminescence found for many organic and inorganic compounds, "low energy" pressure waves (for example, due to gentle, hand grinding) in crystals generate excited electronic states, even if parent molecular emission is not directly observed. Parent molecule emission (i.e., classical triboluminescence) can be quenched as electronic to vibrational energy, through ultrafast, nonadiabatic, conical intersections (e.g.,  $S_n$  to  $S_0$ ), evolves. This phenomenon, in a condensed phase or an isolated molecule, occurs to generate dominant local ultrafast molecular kinetics even in the presence of relatively strong van der Waals (e.g., hydrogen bonding, ca. 40 kJ/mol) condensed phase interactions because intramolecular vibrational coupling is larger than intermolecular molecule phonon coupling.<sup>42–44</sup> Even for the energetic salts of interest in this study, the ions comprising the salt interact more strongly than the neighboring ions do, as appears clear from the published crystal structure results.<sup>1,2</sup>

Thereby, the isolated molecule experiments and theory represent a reasonable approximation to the primary initial behavior for the decomposition of energetic molecules, salts, and in general condensed phase materials. In this case, conical intersections, which are the crossing and interaction point between two electronic states, play a key role in the ultrafast ( $\sim 100$  fs) decomposition mechanisms.<sup>28,45–47</sup> In our previous study of energetic molecules, the existence of conical

intersections provides a direct, nonadiabatic, decomposition pathway from the excited state to the ground state, which successfully explains the experimental observations. In addition to the ground state decomposition through conical intersections, molecules can also decompose directly on the excited state potential energy surface. On the basis of our previous studies<sup>40,41</sup> and through comparison of the energetic barriers for different decomposition paths, energetic materials decompose on their ground electronic state surfaces such that all their acquired electronic excitation energy is utilized to break bonds as observed in the experiments, through product energy distributions and content. The presented discussion includes product energy distribution, at the initial ultrafast molecular level, following electronic excitation for the isolated energetic salts of interest. Of course, completely ground state processes can occur, but in most instances do not generate the observed products, and energy distributions within the products, on an ultrafast time scale.<sup>52</sup>

On the basis of the CASSCF and DFT calculated ground electronic state minimum energy structures of single gas phase or crystal TKX-50 and MAD-X1 molecules, the distinction between ionic and hydrogen bonded species is not easily drawn. The defining feature for this distinction, assuming it is indeed required, is thereby the charge densities on the different moieties composing the individual species in both minimum energy environments and conformations. The charge density results, which will be discussed in detail later in the Theoretical Results and Discussion section, strongly support the notion that even for the isolated molecular system these species are still basically salt-like, ionic compounds. Also in this case, we still term these energetic species salts in order to reference them consistently with their previously published studies: whether these two energetic materials are called or considered as ionic (salts) or hydrogen bonded compounds does not affect our calculational results, which are of course founded only on structural and energetic grounds irrespective of how one labels the final charge densities.

The previously reported energetic materials are for the most part organic molecules with NO<sub>2</sub> groups bonded to a carbon or nitrogen atom.<sup>28–40,46</sup> From those studies, the initial step in the decomposition process following electronic excitation of the isolated molecules is X–NO<sub>2</sub> (X = C,N) to X–ONO isomerization (a nitro-to-nitrite, unimolecular reaction): the isomerized species then decomposes to form an NO product on the ground electronic state potential energy surface (PES) of the energetic species. As TKX-50 does not have an NO<sub>2</sub> group in its structure, a totally different decomposition mechanism will be found in this work.

In sum, in our experimental study, energy resolved spectra are studied to define the initial decomposition dynamics of the energetic salt isolated molecule through elucidating the rotational and vibrational temperatures of the decomposition product NO and the rotational temperature of another product N<sub>2</sub>. Theoretically, by employing quantum chemistry calculations (Gaussian 09, CASSCF), potential energy surfaces for the excited state and the ground electronic state are explored. The detailed decomposition mechanisms of TKX-50 and MAD-X1 molecular ions are thereby determined and discussed. This is the first time the decomposition mechanisms of energetic salts are studied both theoretically and experimentally. As TKX-50 does not contain a NO<sub>2</sub> group, a new ring opening mechanism is proposed. We provide a detailed comprehension of these ionic energetic species decomposition

mechanisms and thereby generate insights into their behavior as energetic materials.

The calculations afford predictions for energies, structures, conical intersections, product species, and product energy distributions. The experimental observations (initial products, product energies, and their internal energy distributions) can only be compared to a given theoretical potential energy surface or reaction channel for these properties and in this regard the calculations are quantitative and predictive. However, because the theoretical structures and energies of transition states and conical intersections cannot be measured and observed in the present experiment, consequently one cannot unequivocally state that the calculations are quantitatively accurate for this part of the mechanism or reaction channel.

## II. EXPERIMENTAL PROCEDURES

The experimental setup consists of a matrix-assisted laser desorption (MALD) system, a supersonic jet expansion nozzle, and a time-of-flight mass spectrometer. Details of the instrumental design are described in our previous papers.<sup>29,30,48,49</sup> The nozzle used for the molecular beam generation is constructed from a Jordan Co. pulsed valve and a laser ablation attachment. The laser desorption head is attached to the front of the pulsed valve with three significant parts: (1) a 2 × 60 mm channel for the expansion gas from the nozzle, (2) a conical channel (3 mm at the outside and 1 mm at the intersection with gas expansion channel) for the ablation laser beam perpendicular to the expansion gas channel, and (3) a 40 mm diameter hole for the sample drum. The sample drum fits into the 40 mm hole and is simultaneously rotated and translated by a motor and gear system in the vacuum in order to present a fresh sample region to the ablation laser for each pulse. The nonvolatile samples are desorbed from the drum by 532 nm ablation laser, entrained in the flow of He carrier gas under a pressure of 80 psi through the 2 × 60 mm channel in the laser desorption head and expanded into the vacuum chamber. With 80 psi He backing pressure for the closed pulsed valve, the chamber pressure remains  $8 \times 10^{-8}$  Torr; with the valve open at 10 Hz, the chamber pressure increases to  $4 \times 10^{-7}$  Torr.

All sample drums for MALD are prepared by wrapping a piece of porous filter paper around a clean Al drum. A solution of 0.02 mol/L matrix (rhodamine 6G) and 0.02 mol/L sample in water is uniformly sprayed on the drum surface while it is rotating under a halogen heat lamp in a fume hood to make sure the sample coating is dry. An air atomizing spray nozzle (Spraying System Co.) with siphon pressure of 10 psi is used to deposit sample plus matrix on the filter paper surface. The dried drum with well-distributed sample is then placed in the laser ablation head assembly and put into the vacuum chamber for decomposition reaction studies. Both TKX-50 and MAD-X1 are supplied by Prof. Thomas M. Klapökte, Ludwig–Maximilian University of Munich.

Laser ablation of any molecular, covalent, or ionic solid will generate both ionic and neutral species. Ablation of salts will, in general, yield neutrals and some ionic components, as well as any ions created by the ablation process. In addition to the ablation laser, one or two other lasers are required to photoexcite the sample in the beam and then detect the dissociated fragments. In our apparatus, only the neutrals can enter the electric field extraction/ionization region because the plates are continuously charged to 4.0 and 3.75 kV, as is usual

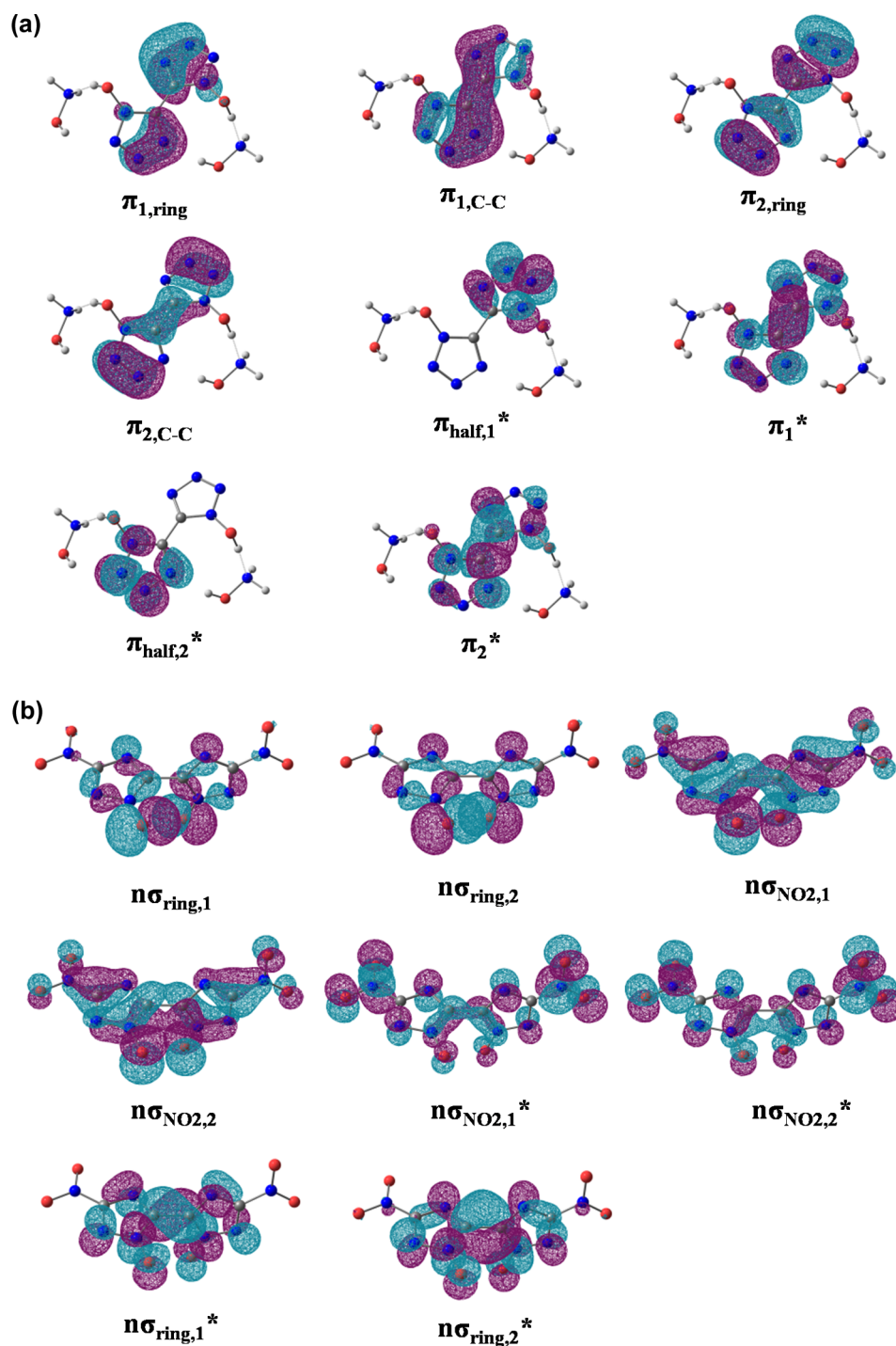


**Figure 2.** (a) Orbitals used in the active space of CASSCF calculations for TKX-50. The (8,8) active space comprises bonding and antibonding  $\pi$  orbitals. (b) Orbitals used in the active space of CASSCF calculations for MAD-X1 dianion. The (8,8) active space comprises nonbonding  $\sigma$  orbitals. For atoms in the structure, gray is carbon, blue is nitrogen, red is oxygen and white is hydrogen.

for a linear 1 m time-of-flight mass spectrometer with a three plate ion focusing region for laser ionization of neutrals. Negative ions entering this region are attracted to the high voltage plate and are not deflected toward the flight tube/detector, and positive ions undergo a curved deflection as they enter the high voltage field region and do not reach the microchannel detector at all or are dispersed by the field to generate only a background signal, which is known to be quite small (<1 mV) by measurement. Moreover, the structures of TKX-50 and MAD-X1 reported<sup>1,2</sup> are clearly composed of the

compounds indicated, ionically attracted to their charged partners, and held together by van der Waals forces for the most part to their molecular neighbors.

A single pump/probe laser is used at 226/236/248 nm for initiation of the energetic sample decomposition and detection of the NO product.  $\text{NO}^+$  is generated by a one color (1 + 1) resonance-enhanced two photon ionization (R2PI) scheme [ $A(v' = 0) \leftarrow X(v'' = 0-2)$  and  $I \leftarrow A$  transitions] and is observed through time-of-flight mass spectrometry (TOFMS). The proper UV laser wavelengths for this process are generated

by a dye laser, pumped by the second harmonic (532 nm) of a Nd: yttrium aluminum garnet laser's fundamental output (1.064  $\mu\text{m}$ ), in conjunction with a wavelength extension system. The typical pulse energy of the UV laser is 70–700  $\mu\text{J}$ /pulse, which gives an intensity of  $\sim 2.0 \times 10^7$  to  $2.8 \times 10^8$   $\text{W}/\text{cm}^2$  for a 8 ns pulse duration. The spectra are not saturated and only single photon absorption occurs at each resonant transition for the sample and the NO product at ca. 50  $\mu\text{J}$ /pulse between 248 and 226 nm. The molecular beam is perpendicularly crossed by the UV laser beam, which is focused to a spot size of about 0.2 mm diameter at the ionization region of the TOFMS.

For  $\text{N}_2$  detection, a single pump/probe laser is used at 283 nm for both sample initiation and  $\text{N}_2$  detection following a one color (2 + 2) resonance-enhanced four photon ionization (REMPI) scheme [ $a^1\Pi_g(v' = 1) \leftarrow X^1\Sigma_g(v'' = 0)$  and  $I \leftarrow a$  transitions] through TOFMS.<sup>50–52</sup> The UV laser wavelength for  $\text{N}_2$  detection is generated by the same dye laser and frequency doubling system as employed for NO detection minus the frequency mixing process. As four photons are required in one detection, the typical pulse energy of the UV laser is about 10–100 times higher than that employed for NO detection (ca. 6–7 mJ/pulse), giving an intensity of  $\sim 2.4 \times 10^9$  to  $2.8 \times 10^9$   $\text{W}/\text{cm}^2$  for a 8 ns pulse duration. Before the detection of  $\text{N}_2$  from energetic materials, a 3%  $\text{N}_2$  in He gas mixture is prepared and studied for the calibration of  $\text{N}_2$  rotational spectrum.

The timing sequence of pulsed nozzle, ablation laser, and excitation/ionization laser is controlled by time delay generators (SRS DG535). The experiment is run at a repetition rate of 10 Hz. Ion signals in the TOFMS are detected by a microchannel plate (MCP), and signals are recorded and processed on a personal computer (PC) using an ADC card (Analog Devices RTI-800) and a boxcar averager (SRS SR 250).

Since no experimental data exist for vertical excitation energies of TKX-50 and MAD-X1 molecules, in order to determine the accuracy of theoretical calculation in the higher electronic states, the experimental UV–vis absorption spectra of these two energetic salts are taken through UV–vis–NIR Varian Cary 500 spectrometer. These spectra are discussed in section IV.

### III. COMPUTATIONAL METHODS

Most calculations are executed at the CASSCF(8,8)/6-31G(d) level of theory within the Gaussian 09 program. To explore the excited state potential energy surfaces, the active space comprises eight electrons distributed in eight orbitals, denoted as CASSCF(8,8). No symmetry restrictions are applied for the calculations. For the TKX-50 calculation, equilibrium geometry calculations are conducted taking the total charge as neutral and the spin multiplicity as 1 ( $S = 0$ ). Orbitals used for the TKX-50 active space are two  $\pi$ -bonding orbitals around the C–C bond between the two tetrazole rings  $\pi_{1,\text{C-C}}$  and  $\pi_{2,\text{C-C}}$ , two  $\pi$  orbitals around the bistetrazole rings  $\pi_{1,\text{ring}}$  and  $\pi_{2,\text{ring}}$ , two delocalized  $\pi$ -antibonding orbitals around the whole molecular system  $\pi_1^*$  and  $\pi_2^*$ , and two  $\pi$ -antibonding orbitals on each of the tetrazole rings  $\pi_{\text{half},1}^*$  and  $\pi_{\text{half},2}^*$  as shown in Figure 2a. To balance the accuracy and calculational efficiency, the negative 3,3'-dinitro-5,5'-bis-1,2,4-triazole-1,1'-diol dianion (MAD-X1 dianion) is used for the theoretical study instead of MAD-X1 salt. The MAD-X1 dianion is employed to simplify the MAD-X1 calculation, as the calculations predict the observed

dynamics and products for decomposition. Details of this approach will be examined in the Theoretical Results and Discussion section and shown in the Supporting Information. Equilibrium geometry calculations are conducted taking the total charge as  $-2$  and the spin multiplicity as 1 ( $S = 0$ ). Orbitals used for the MAD-X1 dianion active space are shown in Figure 2b. They include four  $\sigma$ -nonbonding orbitals around the bistriazole rings  $n\sigma_{\text{ring},1}$ ,  $n\sigma_{\text{ring},2}$ ,  $\sigma_{\text{ring},1}^*$ , and  $\sigma_{\text{ring},2}^*$  and four  $\sigma$ -nonbonding orbitals on the whole molecule  $\text{NO}_2$  groups  $n\sigma_{\text{NO}_2,1}$ ,  $n\sigma_{\text{NO}_2,2}$ ,  $n\sigma_{\text{NO}_2,1}^*$ , and  $n\sigma_{\text{NO}_2,2}^*$ . These orbitals are chosen because they span the orbital space from HOMO  $-3$  to LUMO  $+3$  and cover the whole structure for both the TKX-50 neutral and MAD-X1 dianion. The HOMO  $-3$  to LUMO  $+3$  orbitals for TKX-50 are mainly  $\pi$  orbitals, while for the MAD-X1 dianion they become  $\sigma$ -nonbonding orbitals. This difference may arise because TKX-50 is a neutral molecule, while MAD-X1 dianion has a  $-2$  charge. CASMP2 is applied as the correction for all the CASSCF calculated energies. The ZEP difference between  $S_0$  and  $S_1$  is small and is not essential here.

Excitation energies are calculated by state averaging over the ground and excited states with equal weights for each state. For the TKX-50 calculation, B3LYP/6-31g(d) is also applied to compare with the CASSCF results, in order to ensure that the CASSCF calculation results are reasonable considering the specific orbital choice. For the MAD-X1 calculation, B3LYP/6-31g(d) is applied for the ground state of the complete salt to verify that the MAD-X1 dianion represents a sufficient description of the theoretical reaction properties of the energetic material. The CASSCF results have to be used as the basis of the discussion because conical intersections between the ground and first excited state are the most important points on the decomposition potential energy surface (reaction channel). Through conical intersections, a molecule can move from excited electronic state to the ground state storing huge amounts of energy in the vibrational degrees of freedom. The CASSCF, or similar closely related algorithms, is the only current method to give information on conical intersections. Larger basis sets than 6-31(d) for CASSCF calculations do not substantially improve the results and understanding of the reaction mechanisms.<sup>38</sup> The calculational results for TKX-50 dianion, employing basis sets 6-31g(d) and 6-31+g(d), are compared in the Supporting Information (Table S1): the energy difference for these two basis set calculations is within 0.1 eV. Therefore, addition of a diffuse orbital does not make a difference in the basic derived mechanism calculated for molecular decomposition using a CASSCF algorithm, consistent with previous reports.

Critical points (minima and transition state structures) are characterized by analytical frequency calculations, and minimum energy paths are calculated using an intrinsic reaction coordinate (IRC) algorithm implemented in the Gaussian 09 program suite.<sup>53–56</sup> To find the transition and intermediate states along the reaction pathways, a relaxed scan optimization algorithm as implemented is employed in which all geometrical parameters except for the specified bond distance are optimized and electronic energies are monitored as the specified bond is elongated. In the scan, the structure with peak potential energy is most likely a transition state, and the structure with potential energy in a valley is most likely an intermediate state. To verify this conclusion and obtain a more accurate potential energy surface for the transition/intermediate states, the molecular structure provided in the scan is used as the initial structure in the following optimization calculation with CASSCF(8,8) as

the active space. For both TKX-50 and the MAD-X1 dianion, the transition state on the first excited state cannot be converged using the CASSCF calculation. At present, the maximum orbitals in CASSCF calculation are 16, and for analytical frequency calculations the maximum is only eight orbitals. For big complicated molecules such as those considered here, eight orbitals are not sufficient to describe the whole molecular orbital picture, and the calculation is extremely expensive, especially for excited states. Therefore, a TD-DFT/6-31g(d) method is applied to find the excited transition state. The transition state energy on the excited electronic state is calculated using the energy difference between the excited transition point from a TD-DFT calculation and the Franck–Condon structure on the ground electronic state also from a DFT calculation. Both TD-DFT and CASSCF are applied to calculate the minimum stable structure of TKX-50 on the  $S_1$  state, and the structures obtained are similar for these two methods. The accuracies of the calculations along the reaction pathway are difficult to estimate since experimental information about the conical intersections and the transition states is not available. The experimental results just provide the decomposition products and their internal temperatures: they cannot give direct information on conical intersections and transition states. So calculations are not quantitative predictions for proving the experimental results; they are qualitative mechanisms showing the big picture for the unimolecular decomposition processes and open reaction channels. This is always the situation with regard to kinetics and dynamics, even for simpler systems. Calculations presented in this article are based on the experimental observations including decomposition products and the internal energy distributions within these products. Therefore, the proposed reaction pathways based on the computational results provide a reasonable and, at minimum, qualitative interpretation for the experimental observations.

#### IV. EXPERIMENTAL RESULTS AND DISCUSSION

**A. UV–Vis Absorption Spectra of TKX-50 and MAD-X1.** The UV–vis absorption spectra of TKX-50 and MAD-X1 are shown in Figure 3: the maximum absorption wavelengths for TKX-50 are 263 and 236 nm, and the maximum absorption wavelengths for MAD-X1 are 369 and 270 nm. For NO

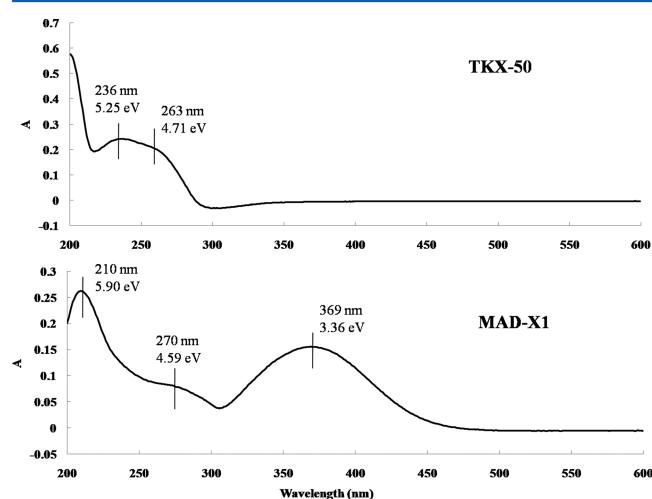


**Figure 3.** UV–vis absorption spectra of TKX-50 and MAD-X1, in  $H_2O$  at ca.  $10^{-5}$  M.

detection, the laser wavelengths are 248–226 nm, which are close to the absorption peaks of TKX-50 and MAD-X1. Therefore, these species are readily excited to higher electronic states by the absorption process. For  $N_2$  detection, the laser wavelength is 283 nm, which is lower in energy than the absorption maximum but still within the absorption band of TKX-50: note too that the laser energy at 283 nm is about 10 to 100 times greater than at ca. 230 nm.

**B. Decomposition Product NO.** Decomposition product NO is observed from electronically excited TKX-50 and MAD-X1 at 226/236/248 nm by TOFMS. The 226/236/248 nm excitation wavelengths also correspond to the resonance  $(0-0)/(0-1)/(0-2)$  vibronic bands of the  $A^2\Sigma^+ \leftarrow X^2\Pi$  electronic transition of the NO product. Therefore, by scanning these laser excitation wavelengths, a  $(1+1)$  R2PI rotationally resolved spectrum of the NO product from TKX-50 or MAD-X1 is obtained. The line width of the NO mass peak is 10 ns (the laser pulse width), consistent with that expected for decomposition from the lowest few excited states. If the two energetic salts were to absorb two or more photons sequentially, the NO mass signal would broaden as we have reported earlier.<sup>29,31,48,49</sup> Thus, the NO product is associated with single photon absorption for these two samples. In this experiment, laser beam intensity is varied without change in the NO TOFMS line width, so that multiphoton dissociation of TKX-50 or MAD-X1 is unlikely. Excited electronic states of the two energetic salts, which might be generated in the ablation process, are effectively relaxed and cooled in the highly collisional expansion process, through the supersonic nozzle. The arrival time at the ionization/extraction region of the TOFMS for the species generating the NO spectrum is consistent with that of a large mass molecule (ca. 300–350 amu).<sup>29</sup>

Figures 4 and 5 show the spectra of three different  $A(\nu' = 0) \leftarrow X(\nu'' = 0,1,2)$  rovibronic transitions of the NO molecule generated from TKX-50 and MAD-X1 excited to its first excited

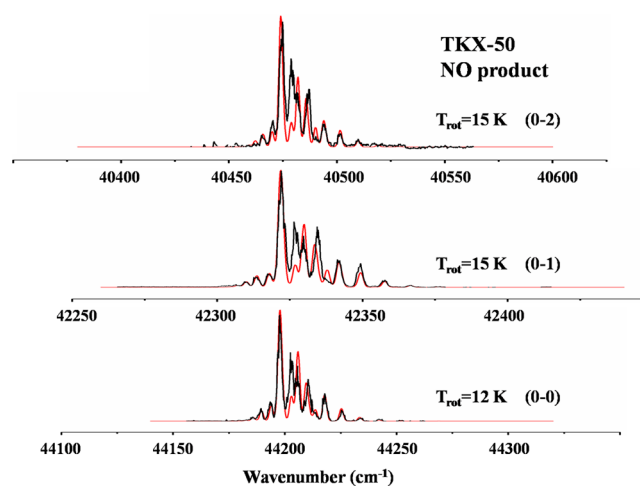


**Figure 4.** One color  $(1+1)$  R2PI spectra of the vibronic transitions  $A^2\Sigma^+(\nu' = 0) \leftarrow X^2\Pi(\nu'' = 0,1,2)$  of the NO product following electronic state excitation of TKX-50. Rotational simulations with a Boltzmann population distribution show that the rotational temperatures of three observed vibrational levels of the ground electronic state of NO  $(0-0)$ ,  $(0-1)$ , and  $(0-2)$  are 12, 15, and 15 K, respectively, with  $\pm 10$  K uncertainty. The black line is the experimental data, and the red one is the theoretical simulation for NO  $(A-X)$  transition at rotational temperatures 12 or 15 K.

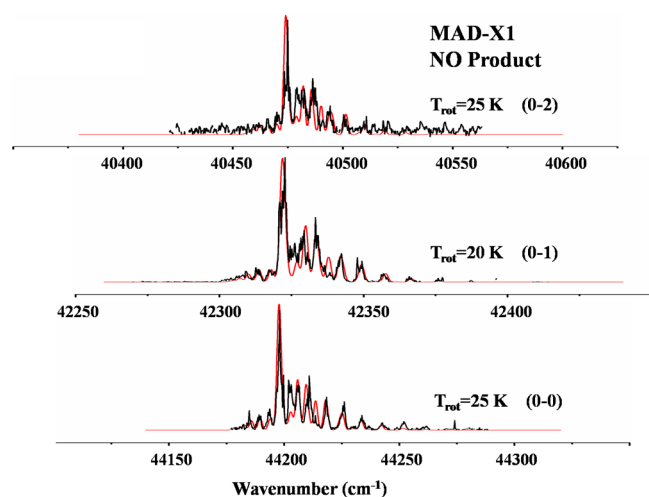


**Figure 5.** One color (1 + 1) R2PI spectra of the vibronic transitions  $A^2\Sigma^+(v' = 0) \leftarrow X^2\Pi(v'' = 0,1,2)$  of the NO product following electronic state excitation of MAD-X1. Rotational simulations with a Boltzmann population distribution show that the rotation temperatures of the three observed vibrational levels on the ground electronic state of NO (0–0), (0–1), and (0–2) are 25, 20, and 25 K, respectively, with  $\pm 10$  K uncertainty. The black line is the experimental data, and the red one is theoretical simulation for NO (A–X) transition at rotational temperatures 25 or 20 K.

electronic state. All spectra have similar rotational patterns but a varying vibrational intensity for each vibronic band. The most intense feature in each spectrum of NO corresponds to the ( $Q_{11} + P_{12}$ ) band, and the lower intensity features for each vibronic transition correspond to other rotational transitions.<sup>57</sup> The rotational temperatures from spectral simulations based on Boltzmann population distributions for the three vibronic transitions of the NO product from TKX-50 are  $(12 \pm 10)$  K,  $(15 \pm 10)$  K, and  $(25 \pm 10)$  K for the three vibrational levels ( $v'' = 0,1,2$ ) in the ground electronic state of NO. For MAD-X1, the rotational temperatures of NO products for the three vibrational transitions ( $v'' = 0,1,2$ ) are  $(25 \pm 10)$  K,  $(20 \pm 10)$  K, and  $(25 \pm 10)$  K, respectively. Some experimental data are not exactly fit with the simulations because (1) laser intensity is only stable to about 10%, (2) sample spraying is not perfectly uniform and the concentration of material on the filter paper is not always constant, and (3) purity of the rhodamine 6G may affect the final result.

The vibrational temperature of the NO product can be obtained by simulating the relative intensities among the observed vibronic bands, using a Boltzmann population distribution analysis and the Franck–Condon factors.<sup>40</sup> The vibrational temperature of the NO product from TKX-50 and MAD-X1 are calculated to be  $(2600 \pm 250)$  K and  $(1500 \pm 250)$  K, respectively. Details of the vibrational temperature calculation are described in our previous paper.<sup>40</sup> In summary, the NO product from electronically excited TKX-50 and MAD-X1 has a low rotational temperature and a hot vibrational temperature, which is similar to our previous results for energetic molecules with NO<sub>2</sub> groups. The NO vibrational temperature from TKX-50 is 1100 K higher than from MAD-X1, due most likely to the different NO formation mechanisms. For TKX-50, NO product is released from the amine N-oxide part of the tetrazole ring, while for MAD-X1, NO product is from the nitro group. The vibrational temperature comparison of NO products between TKX-50 and MAD-X1 will be

discussed further in the Theoretical Results and Discussion section.

Even though the MALD technique is known to desorb fragile molecules to the gas phase without fragmentation, we have shown the NO product, in our previous studies, to be created in the apparatus excitation region (i.e., the reaction/ionization/extraction region of the TOFMS).<sup>29</sup> In our experimental system, the MALD process is limited to just sample ablation: the decomposition of the energetic molecules takes place at the reaction/excitation/extraction region. The laser light used in the MALD process is 532 nm, and the laser for sample decomposition and the excitation laser light is 226–283 nm. The wavelength of 532 nm is not energetic enough for the energetic salt decomposition, but does decompose the matrix. If the salt decomposes in the MALD process, the arrival time for the decomposition products N<sub>2</sub>/NO at the excitation region should be much sooner than that for the parent molecules; however, in our experimental system, this arrival time changes with the mass and collision cross sectional area of the salt or other energetic molecular species. Different salt molecules arrive at the excitation region in different times and are decomposed in that region forming N<sub>2</sub>/NO.<sup>29</sup>

NO product can be produced from several possible pathways in MAD-X1, including N–O bond breaking after a nitro–nitrite isomerization, NO<sub>2</sub> photolysis, and HONO elimination. In our previous study of NO<sub>2</sub> photolysis, the rotational temperature of the NO product from expansion cooled NO<sub>2</sub> gas is 100–300 K hotter than the rotational temperature of the NO product from MAD-X1; thus, NO<sub>2</sub> is not the precursor for the observed NO product, and NO<sub>2</sub> loss is not the major decomposition reaction channel.<sup>29,32–34</sup> The observed rotational and vibrational temperatures assigned for NO in these experiments show clearly that the NO must come from decomposition of the energetic salt and not NO<sub>2</sub>. HONO is also one of the possible intermediates in the formation of NO from MAD-X1. HONO elimination for previously studied X–NO<sub>2</sub> system is less than 5% of the total NO elimination following the nitro–nitrite isomerization; moreover, the rotational temperature of NO product from HONO photolysis is extremely high.<sup>29,32</sup> Thus, neither the NO<sub>2</sub> loss channel nor the HONO channel is present as a competitor to the nitro–nitrite isomerization/NO elimination channel in MAD-X1 following its electronic excitation.

**C. Decomposition Product N<sub>2</sub>.** Decomposition product N<sub>2</sub> is observed from electronically excited TKX-50 and MAD-X1 at 283 nm by TOFMS. The 283 nm excitation wavelength corresponds to the resonance (1–0) vibronic band of the  $a^1\Pi_g \leftarrow X^1\Sigma_g$  electronic transition of the N<sub>2</sub> product. REMPI (2 + 2) rotationally resolved spectra of the N<sub>2</sub> product from TKX-50 and MAD-X1 are obtained by scanning the laser excitation wavelength. The line width of the N<sub>2</sub> mass peak is 10 ns (the laser pulse width) and laser beam intensity is varied without change in the N<sub>2</sub> TOFMS line width. Excited electronic states of the two energetic salts, which might be generated in the ablation process, are effectively relaxed and cooled in the highly collisional expansion process, through the supersonic nozzle.

Figure 6 shows the spectra of  $a^1\Pi_g(v' = 1) \leftarrow X^1\Sigma_g(v'' = 0)$  rovibronic transition of the N<sub>2</sub> molecule from a 3% N<sub>2</sub>/He mixture, and TKX-50 and MAD-X1 excited to their first excited electronic state. The rotational spectra of N<sub>2</sub> from the N<sub>2</sub> gas mixture and the two energetic salts have similar rotational patterns: the most intense peak in each spectrum of N<sub>2</sub> corresponds to the S<sub>0</sub> peak in the S branch rotational

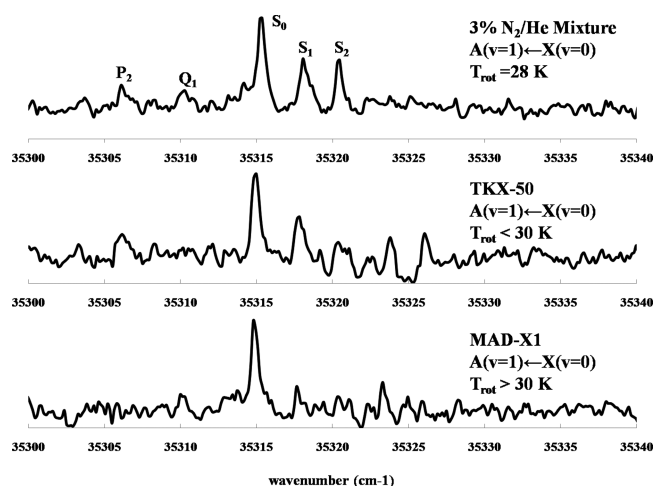


**Figure 6.** (a) One color (2 + 2) REMPI spectra of the vibronic transitions  $a^1\Pi_g(v' = 1) \leftarrow X^1\Sigma_g(v'' = 0)$  of  $N_2$  from a 3%  $N_2/He$  mixture and from electronic state excitation of TKX-50 and MAD-X1. The rotational temperature of the 3%  $N_2$  mixture calculated from a Boltzmann plot equals 28 K. The rotational temperatures of  $N_2$  decomposition products from (b) TKX-50 and (c) MAD-X1 (as indicated) are estimated to be smaller than 30 K.

transitions. Other peaks including  $S_1$  and  $S_2$  peaks in the S branch,  $Q_1$  peak in the Q branch, and the  $P_2$  peak in the P branch rotational transitions are labeled in Figure 6.<sup>51,52</sup> The rotational spectrum for the  $N_2$  mixture expansion is similar to that of previous studies of other groups, indicating a rotational temperature around 20 K. The rotational temperature can also be calculated by a Boltzmann plot using the S branch rotational transition. The rotational line intensity in (2 + 2)  $N_2$ -REMPI spectra is given as

$$I(J', J'') = Cg(J'')S(J', J'') \exp(-E_{rot}/kT_{rot})$$

in which  $C$  is a constant independent of the rotational quantum number of the ground and the resonance state ( $J'$  and  $J''$ , respectively) and  $g(J'')$  is the nuclear spin degeneracy (for  $N_2$ ,  $g = 3$  or  $6$  for odd/even  $J''$ , respectively).  $S(J', J'')$  is the rotational transition strength (two-photon Hönl-London factor), and for the  $S(\Delta J = 2)$  branch of the  $N_2$   $a^1\Pi_g \leftarrow X^1\Sigma_g$  transition,  $S = M(S)J'(J' + 1)J''(J'' + 3)/15(2J'' + 3)$ .  $M(S)$  is transition dipole factor and it has a constant value here.  $T_{rot}$  is the rotational temperature, and  $E_{rot}$  is the rotational energy. For a plot of  $\ln(I/gS)$  vs  $E_{rot}/k$ , the derived slope equals  $-T_{rot}^{-1}$  (Boltzmann plot).<sup>58</sup> From this calculation, the rotational temperature of 3%  $N_2/He$  mixture is about 28 K.

The  $N_2$  signals from the energetic salts are much less intense than those of the  $N_2$  gas mixture, as only the  $S_0$  peak can be consistently observed in the rotational spectra. Therefore, through comparison to the spectrum of the  $N_2$  gas mixture and previous studies,<sup>50–52</sup> the rotational temperatures of the  $N_2$  product released from both TKX-50 and MAD-X1 are lower than 30 K. This is the same result as found for the NO spectra derived from energetic materials in previous studies: again emphasizing that the product molecule (NO or  $N_2$ ) is generated at the ionization/extraction region under unimolecular collision free conditions.

To find the vibrational temperature of the  $N_2$  product, the rotational spectra of  $N_2$  should be obtained for several vibronic bands. The signal intensity of the reported  $N_2$  rotational transition from ground rovibronic state  $v = 0$  is ca. 80 mV,

about 4 times higher than the noise level. To get  $N_2$  rovibronic transition spectra starting from  $v'' \geq 1$  of the ground electronic state, the signal intensity should be 5–10 times lower than the above 80 mV, which is under the detection limit for this measurement. Consequently, further  $N_2$  rovibronic bands were not obtained in these experiments, and thus no vibrational temperature is determined for the  $N_2$  products.

TOF mass spectra, obtained under 283/226 nm excitation employed especially for NO or  $N_2$  detection, display a few very weak additional features in the low mass region. Compared to the NO signal, however, these features are much weaker, and their intensity remains constant as the excitation wavelength is scanned. These additional weak features are most likely not a result of a major decomposition pathway for either of the salt molecules.

## V. THEORETICAL RESULTS AND DISCUSSION

Experimental results yield that NO and  $N_2$  molecules are initial nanosecond  $S_1/S_2$  excitation decomposition products for the electronically excited energetic salt systems under study. In order to understand the experimental data more completely and derive reactions mechanisms, theoretical calculations of (gas phase) molecular geometries and energies for the Franck–Condon structure, conical intersections, transition states, and intermediate states along both the ground and excited state potential energy surfaces are performed for the two energetic salts TKX-50 and MAD-X1. The calculational algorithm employed for these studies reproduces the experimental observations with regard to product generation and energy distribution for each product molecule. This is all one can require of a chosen calculational method: the calculations predict or generate the observed behavior. The approach to calculation of the reaction mechanism (based on the above presented algorithm and approximations) is justified, thereby, by the results of the calculations with regard to product molecules, their energy dynamics and distributions, and the overall reaction kinetics. For the gas phase ground state Franck–Condon structures of TKX-50, as shown in Figure 7, four possibilities are considered. The 5,5'-bistetrazole-1,1'-diolate dianion has negative charges on each oxygen atom of the amine N-oxide moieties, and the hydroxylammonium cation has two kinds of positive hydrogen atoms: one is bonded

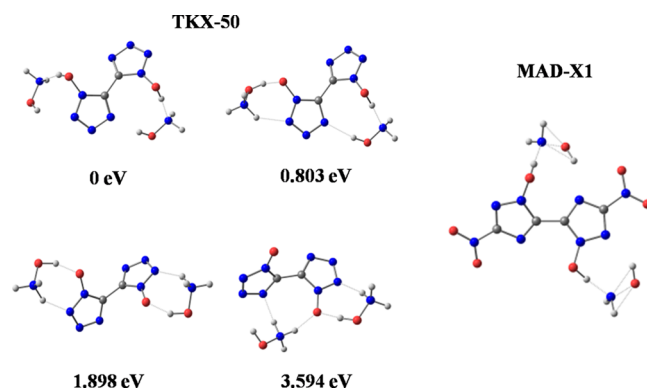


**Figure 7.** Energy comparison of gas phase ground state TKX-50 in four possible structures and for the MAD-X1 gas phase, ground state, minimum energy structure. Calculation for both molecules are at the CASSCF level. Optimization begins at the crystal structure geometry. For atoms in the structure, gray is carbon, blue is nitrogen, red is oxygen, and white is hydrogen.

to the nitrogen atom, the other is bonded to the oxygen atom. The negative oxygen on the dianion can bond with either positive hydrogen on the cation to form hydrogen bonds. From our calculations, the lowest energy ground state structure has both negative oxygen atoms of the dianion bonded to the hydrogen atoms on the ammonium moiety of the cations: this is the TKX-50 structure used as the Franck–Condon structure shown in Figure 7 (0 eV). Furthermore, the most stable gas phase structure of the MAD-X1 neutral salt based on the theoretical calculation has a similar structure to that of TKX-50, except for different dianion rings.

The calculated most stable, single molecule ground state structure of MAD-X1 is shown in Figure 7 as well. For the ground state structures of TKX-50 and MAD-X1, the calculated structures do not clearly address the issue of whether they should be considered ionic salts or hydrogen bonded compounds: as pointed out in the Introduction, the calculated charge density for each of the separate moieties composing these energetic species makes clear that in both compounds and in both structural environments they are ionic and similar in large measure. These charge densities are given as +0.572 and +0.546 for the two  $\text{NH}_3\text{OH}$  moieties and  $-1.118$  for the bistetrazole ring of isolated TKX-50. For isolated MAD-X1, the charge densities of  $\text{NH}_3\text{OH}$  moieties are +0.563 and +0.582, respectively, while the density of the bistetrazole ring is  $-1.145$ . Details of charge densities of gas phase TKX-50 and MAD-X1 compared with their crystals are shown in Figure S1. We use the term salt for both molecules in either environment, in order to be consistent with their previous study; but whatever they are called does not affect the calculational results because TKX-50 is calculated as a whole molecule including all the hydrogen bonds among the two  $\text{NH}_3\text{OH}$  moieties and bistetrazole ring. The decomposition of TKX-50 creating  $\text{N}_2$  and NO as observed in the experiment occurs on its bistetrazole ring; thus, the types of bonds among the  $\text{NH}_3\text{OH}$  groups and bistetrazole ring are not the main issue or concern for this study. For MAD-X1, because the initial molecule is too complicated, we simplify the calculation based on the MAD-X1 dianion. This simplification is proven to be reasonable, as will be explained in detail later in this section. The theoretical reaction paths with potential energies and molecular geometries are shown in Figures 8–15.

Two possible decomposition mechanisms are explored in the theoretical study through two different conical intersections between the  $S_1$  and  $S_0$  states, as mandated by the experimental observations. For TKX-50, the two conical intersections are related to two different tetrazole ring opening positions; for MAD-X1, one conical intersection leads to the opening of the triazole ring, and the other generates formation of a nitro–nitrite isomerization transition state. These two channels are chosen because they are energy available and accessible for the creation of both NO and  $\text{N}_2$  products. The actual reaction pathway will depend on different factors, for example, the rate of internal vibrational energy redistribution, the heights of reaction barriers, and the rate of nonadiabatic transition through the different conical intersections.

Because the CASSCF calculation has a general limitation for the number of orbitals comprising the active space and energetic salts are complicated large molecules, approximate, reduced model calculations need to be considered. The initial structure for TKX-50 can be calculated as a whole molecule, but the MAD-X1 dianion is chosen to find the decomposition mechanism for the MAD-X1 molecule. To be persuaded that

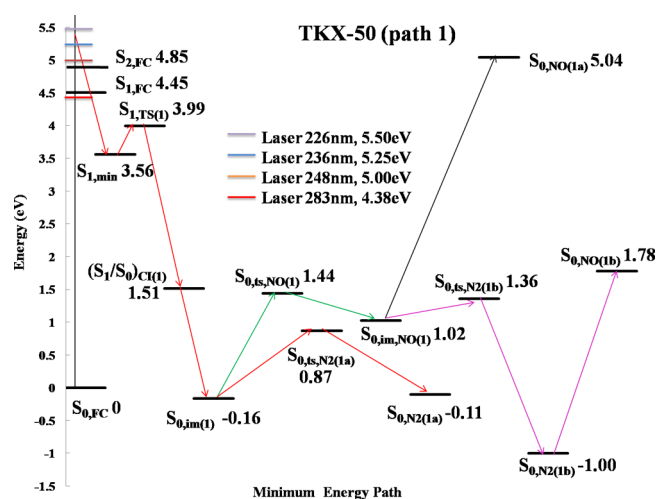


**Figure 8.** Schematic one-dimensional projection of the multidimensional energy surfaces for one of the TKX-50 dissociation paths computed at the CASSCF(8,8)/6-31G(d) level of theory. This reaction path is related to the opening of tetrazole ring between N1 and N2 atoms. The red, green, black, and purple arrows represent different reaction channels for  $\text{N}_2$  and NO dissociation.  $S_{0,FC}$  is the optimized minimum energy of TKX-50 on the  $S_0$  state, and with hydrogen bonds in the system, it is almost planar.  $(S_1/S_0)_{CI(1)}$  is the conical intersection between the  $S_0$  and  $S_1$  states related to the ring opening position between N2–N3 (Figure 1), and  $S_{1,TS(1)}$  is the excited transition state on the  $S_1$  surface from the minimum structure  $S_{1,min}$  and the conical intersection.  $S_{0,im(1)}$  and  $S_{0,im,NO(1)}$  are the intermediate states on  $S_0$  after  $(S_1/S_0)_{CI(1)}$ , while  $S_{0,ts,NO(1)}$ ,  $S_{0,ts,N2(1a)}$ , and  $S_{0,ts,N2(2a)}$  are the transition states on the  $S_0$  surface following  $S_{0,im(1)}$  in different reaction channels.  $S_{0,NO(1a)}$  and  $S_{0,NO(1b)}$  are NO dissociated products on the  $S_0$  state, and a and b relate to the two reaction coordinate pathways. Similarly,  $S_{0,N2(1a)}$  and  $S_{0,N2(1b)}$  are  $\text{N}_2$  decomposition products on the  $S_0$  state.

the simplification of MAD-X1 as a dianion is appropriate, a comparison of different calculational methods and basis sets for both TKX-50 and MAD-X1 molecules is undertaken. The related information is provided in the Supporting Information in Tables S1 and S2. TKX-50 is calculated as (1) a dianion (labeled as method I), (2) a neutral complex in which  $\text{NH}_2\text{OH}$  moieties are removed and negative O atoms of bistetrazole are bonded with hydrogen atoms (labeled as method H), and (3) initial TKX-50 as a whole molecule (labeled as method W) (see Table S1, Supporting Information). In Table S1, comparison of the results of methods (I), (H), and (W) using basis set 6-31g(d) for TKX-50 yields no substantial or essential differences between these methods: all show similar potential surfaces (albeit not identical) for TKX-50 decomposition. The basic TKX-50 decomposition mechanism is as follows: TKX-50 evolves from its first excited electronic state to the ground state via conical intersections  $(S_1/S_0)_{CI}$ , and then decomposes on the ground electronic state with a hot vibrational temperature for the products. Therefore, simplification of the calculation employing either method (I) or (H) is a reasonable idea: both are of equal value. Similar calculations are undertaken for MAD-X1 and are shown in Table S2, Supporting Information. MAD-X1 is calculated as (1) a dianion (labeled as method I), (2) a neutral complex in which  $\text{NH}_2\text{OH}$  moieties are removed and negative O atoms of bistetrazole are bonded with hydrogen atoms (labeled as method H), and (3) initial MAD-X1 as a whole molecule (labeled as method W). As shown in Table S2 (Supporting Information), similar conclusions are obtained for

MAD-X1 as those reached for TKX-50. On the basis of the data found in Tables S1 and S2 (Supporting Information), one can be confident that such an approach is justified, insightful, and yields a reliable explication of the experimental results.

Calculations at the CASSCF(8,8)/6-31G(d) theoretical level are employed to determine the vertical excitation energies for TKX-50 and MAD-X1 dianion from the ground electronic state  $S_0$  (FC structure) to the first excited state  $S_1$ . The vertical excitation energies of the two energetic materials are very close to the energy of photon excitations in the range from 283 to 226 nm (4.3 to 5.5 eV), which have been used to excite these molecules.

Since data are not available for vertical excitation energies of TKX-50 and MAD-X1 molecules, experimental UV-vis absorption spectra of these two energetic salts are taken to determine the accuracy of the CASSCF calculations. The vertical excitation calculated through CASSCF(8,8)/6-31G(d) for the first and second excited electronic states  $S_1$  and  $S_2$  of TKX-50 are 4.45 and 4.85 eV, respectively. The UV-vis absorption of TKX-50 as shown in Figure 3 contains two peaks at 4.71 and 5.25 eV, while from TD-DFT calculation the energy of  $S_1$  and  $S_2$  states for TKX-50 are 4.88 and 5.27 eV, respectively. This comparison reveals that the CASSCF(8,8) method gives a reasonable treatment of the relevant excited states, as they fall into the commonly acceptable uncertainty range of  $\pm 0.5$  eV. The vertical excitation calculated for the lowest lying excited electronic state  $S_1$  of MAD-X1 is 3.25 eV. The UV-vis absorption of MAD-X1 has a maximum at about 3.36 eV, which also demonstrates that a CASSCF(8,8) method is reasonable for energetic salt  $S_0$ ,  $S_1$ ,  $S_2$  theoretical studies.

For the ground state calculation, both CASSCF and DFT methods are applied for comparison to make sure all the theoretical calculations yield reasonable results. The potential energy surfaces for the  $S_2$  state of these two salts are above the laser excitation maximum. Thus, the  $S_2$  state is not considered in the potential energy surface calculations. The experimental results yield high vibrational and cold rotational temperatures for NO and cold rotational  $N_2$  product temperatures. The calculations must generate decomposition mechanisms for NO and  $N_2$  from TKX-50 and MAD-X1 under the energy limit imposed by the excitation source and the parent molecule internal temperature in the beam: in particular the calculations must explicate product internal temperatures. The present calculational results fulfill these two goals. Additionally, for the decomposition mechanisms of the two energetic salts, only molecular singlet states and singlet-singlet transitions are considered because, on the basis of our previous femtosecond studies of energetic materials RDX and HMX, the decomposition dynamics fall into the time scale of our excitation pulse duration (ca. 100 fs). These results emphasize that energetic material decomposition is an extremely fast, nonadiabatic reaction at the molecular level. Molecular singlet-singlet transitions are much faster than singlet-triplet, spin forbidden transitions. The time scale of molecular fluorescence emission is between  $10^{-5}$  to  $10^{-10}$  s, while that for phosphorescence emission is  $10^{-4}$  s to 10 s. Therefore, singlet-triplet transitions and couplings are not the main energy conversion pathway for these energetic systems.

**A. Calculations for TKX-50.** Schematic one-dimensional projections of the multidimensional singlet potential energy surfaces ( $S_0$  and  $S_1$ ) of TKX-50, with locations and potential energies (the presented energies are not corrected for zero-point energy) for different critical points and conical

intersections along the minimum energy reaction paths, are plotted in Figures 8 and 10. Figures 8 and 10 described the two different reaction mechanisms for TKX-50. The reaction coordinates depicted in Figures 8 and 10 include C-N and N-N bond lengths and O...H and N...H hydrogen bond lengths at the active site of TKX-50, which is at the tetrazole ring close to the amine N-oxide. Arrows in Figures 8 and 10 indicate different possible reaction channels for TKX-50 decomposition. The structures of each critical point and conical intersection are summarized in Figures 9 and 11,

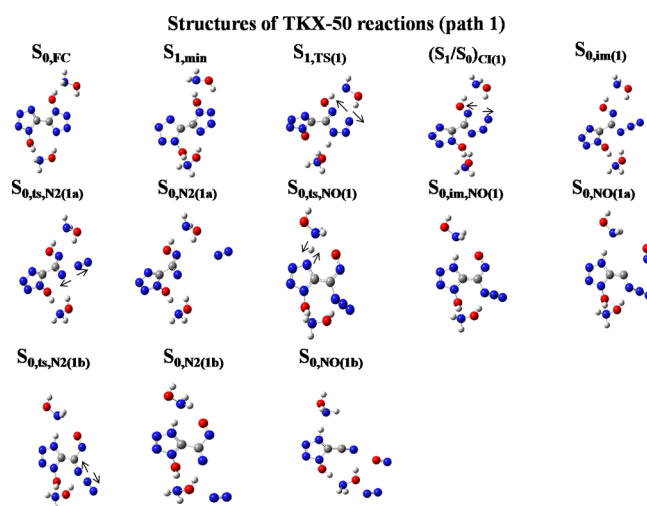


**Figure 9.** Structures of all critical points and conical intersections mentioned in Figure 8 along the TKX-50 dissociation reaction path 1. Arrows in the structures of the transition states show the reaction coordinate associated with the imaginary frequency. For atoms in the structure, gray is carbon, blue is nitrogen, red is oxygen, and white is hydrogen.

respectively. In Figures 8 and 9, FC geometry  $S_{0,FC}$  is the optimized minimum energy of TKX-50 on the  $S_0$  state, and with hydrogen bonds in the system, it is almost planar.  $(S_1/S_0)_{CI(1)}$  is the conical intersection between the  $S_0$  and  $S_1$  states related to the ring opening position between N2-N3 (Figure 1), and  $S_{1,TS(1)}$  is the excited transition state on the  $S_1$  surface between the minimum structure on the  $S_{1,min}$  and the conical intersection. The difference between the TKX-50  $S_0$  and  $S_1$  structures is that one tetrazole ring of TKX-50 in  $S_1$  is bent and nonplanar, while both tetrazole rings of TKX-50  $S_0$  are planar.  $S_{0,im(1)}$  and  $S_{0,im,NO(1)}$  are the intermediate states on  $S_0$  after  $(S_1/S_0)_{CI(1)}$ , while  $S_{0,ts,NO(1)}$ ,  $S_{0,ts,N2(1a)}$ , and  $S_{0,ts,N2(2a)}$  are the transition states on the  $S_0$  surface following  $S_{0,im(1)}$  in different reaction channels.  $S_{0,NO(1a)}$  and  $S_{0,NO(1b)}$  are NO dissociated products on the  $S_0$  state, and a and b are related to the two pathways (mechanisms). Similarly,  $S_{0,N2(1a)}$  and  $S_{0,N2(1b)}$  are  $N_2$  decomposition products on the  $S_0$  state. Figure 10 shows a reaction mechanism pattern close to that of Figure 8, and the subscript of the critical points changes from (1) to (2), as this reaction path system has a different conical intersection  $(S_1/S_0)_{CI(2)}$  between the  $S_0$  and  $S_1$  states related to the ring opening position between C1-N2.

The reaction path in Figure 8 shows that, following excitation to the first excited electronic state  $S_1$ , TKX-50 undergoes a rapid internal conversion from the Franck-Condon structure to the energy minimum structure  $S_{1,min}$  on the  $S_1$  state. Then the molecule encounters a 0.43 eV energy barrier for a transition state  $S_{1,TS(1)}$  and moves to the ground electronic state

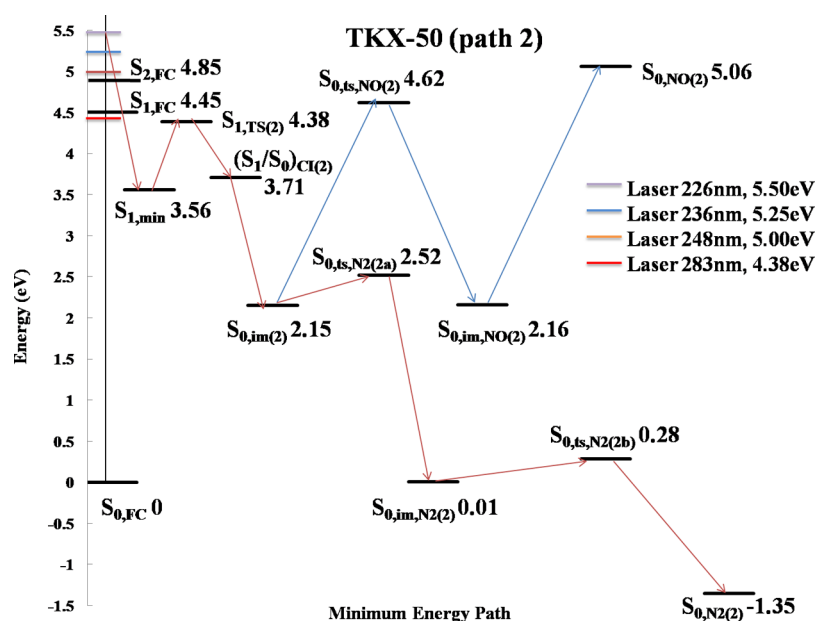


**Figure 10.** Schematic one-dimensional projection of the multidimensional energy surfaces for the other TKX-50 dissociation path 2 computed at the CASSCF(8,8)/6-31G(d) level of theory. This reaction path is related to the opening of tetrazole ring between C1 and N1 atoms. The blue and brown arrows represent different reaction channels for N<sub>2</sub> and NO dissociation. S<sub>0,FC</sub> is the optimized minimum energy of TKX-50 on the S<sub>0</sub> state, and with hydrogen bonds in the system, it is almost planar. (S<sub>1</sub>/S<sub>0</sub>)<sub>CI(2)</sub> is the conical intersection between the S<sub>0</sub> and S<sub>1</sub> states related to the ring opening position between C1–N1 (Figure 1), and S<sub>1,TS(2)</sub> is the excited transition state on the S<sub>1</sub> surface between the minimum structure on the S<sub>1,min</sub> and the conical intersection. S<sub>0,im(2)</sub>, S<sub>0,im,N2(2)</sub>, and S<sub>0,im,NO(2)</sub> are the intermediate states on the S<sub>0</sub> after (S<sub>1</sub>/S<sub>0</sub>)<sub>CI(2)</sub>, while S<sub>0,ts,NO(2)</sub>, S<sub>0,ts,N2(2a)</sub>, S<sub>0,ts,N2(2b)</sub>, and S<sub>0,ts,NO(2)</sub> are the transition states on the S<sub>0</sub> surface following S<sub>0,im(2)</sub> in different reaction channels. S<sub>0,NO(2)</sub> is NO dissociated products on the S<sub>0</sub> state, and S<sub>0,N2(2)</sub> is N<sub>2</sub> decomposition products on the S<sub>0</sub> state.

through the (S<sub>1</sub>/S<sub>0</sub>)<sub>CI(1)</sub> conical intersection: molecules undergoing this process would place sufficient vibrational energy in the S<sub>0</sub> state, transferred from the S<sub>1</sub> electronic energy, to dissociate. The adiabatic energy gap between the S<sub>1</sub> and S<sub>0</sub> surfaces near (S<sub>1</sub>/S<sub>0</sub>)<sub>CI(1)</sub> is computed to be 28 cm<sup>-1</sup>, which means the S<sub>1</sub> and S<sub>0</sub> surfaces are strongly nonadiabatically coupled with one another and the small energy gap (degeneracy) increases the probability of nonadiabatic transition from upper to lower electronic states. The structure of (S<sub>1</sub>/S<sub>0</sub>)<sub>CI(1)</sub> is shown in Figure 9, in which the bond between N2 and N3 atoms is broken and the tetrazole ring opens in the middle. As the molecule moves from the S<sub>1</sub> to S<sub>0</sub> state through (S<sub>1</sub>/S<sub>0</sub>)<sub>CI</sub>, the IRC algorithm shows that the steepest descent pathway for the molecule is to evolve to the stable intermediate state S<sub>0,im(1)</sub>. From S<sub>0,im(1)</sub>, the molecule has two reaction channels and both are energy available. The one shown in red in Figure 8 has the N<sub>2</sub> product dissociating directly from the N<sub>3</sub> moiety of S<sub>0,im(1)</sub>. In this process, the molecule surmounts a 1.03 eV energy barrier for the concerted transition state S<sub>0,ts,N2(1a)</sub> and forms the N<sub>2</sub> product S<sub>0,N2(1a)</sub>. The other channel, shown in green in Figure 8 begins with the hydrogen bond to the NH<sub>3</sub>OH<sup>+</sup> cation: as the molecule moves along the minimum energy reaction coordinate, it encounters a 1.6 eV energy barrier to a transition state, S<sub>0,ts,NO(1)</sub>, along the path from the amine N-oxide to the tetrazole ring to form the intermediate state, S<sub>0,im,NO(1)</sub>. At this point on the minimum energy path, another two possibilities exist for the creation of N<sub>2</sub> and NO products. One path is that the NO group, which is the initial amine N-oxide part of the molecule, dissociates directly from the C–N bond as shown in black in Figure 8. The energy barrier for this process is 4.02 eV, and the energy of the final product is close to the laser energy limit, making the black path unlikely. The other reaction path, shown in purple in

Figure 8, is that N<sub>2</sub> dissociates from the system first with an energy barrier of 0.34 eV from the transition state S<sub>0,ts,N2(1b)</sub>. The molecule with a free N<sub>2</sub> product is labeled as S<sub>0,N2(1b)</sub> in Figure 8. If NO dissociates after N<sub>2</sub> leaves, the energy barrier is 2.78 eV, which is readily surmountable under the experimental conditions. NO and N<sub>2</sub> products move away from the whole molecule without obvious torque for all the reaction channels shown in Figure 8. Therefore, both NO and N<sub>2</sub> products should have low rotational temperatures, as is consistent with the experimental results.

To verify the CASSCF calculation is acceptable, B3LYP/6-31g(d) is also applied for the ground state calculation of TKX-50. The energies of potential surface critical points, based on the TD-DFT method, are given in the Supporting Information in Figure S2, in which energies of conical intersections are calculated as single-point energies using the structures from the CASSCF calculations. In these two calculation methods, most critical points have similar energies and the energy differences is within ±1.0 eV, which is an acceptable range for such a comparison. The accuracy of CASSCF calculations is ±0.5 eV,<sup>59,60</sup> less than 1 eV agreement between two very different quantum chemical algorithms with regard to energies of stationary and critical points on the potential energy surfaces is sufficient to demonstrate the general framework of the decomposition mechanism. Therefore, CASSCF(8,8)/6-31g(d) is a reasonable method for the theoretical study. Larger CASSCF calculations are possible but not with the needed analytical second derivatives within the Gaussian 09 program.

The other reaction path for TKX-50 decomposition is shown in Figure 10. As for the reaction paths in Figure 8, following excitation to the first excited state S<sub>1</sub>, TKX-50 encounters a 0.82 eV energy barrier to a transition state S<sub>1,TS(2)</sub> and goes to the ground electronic state through conical intersection (S<sub>1</sub>/

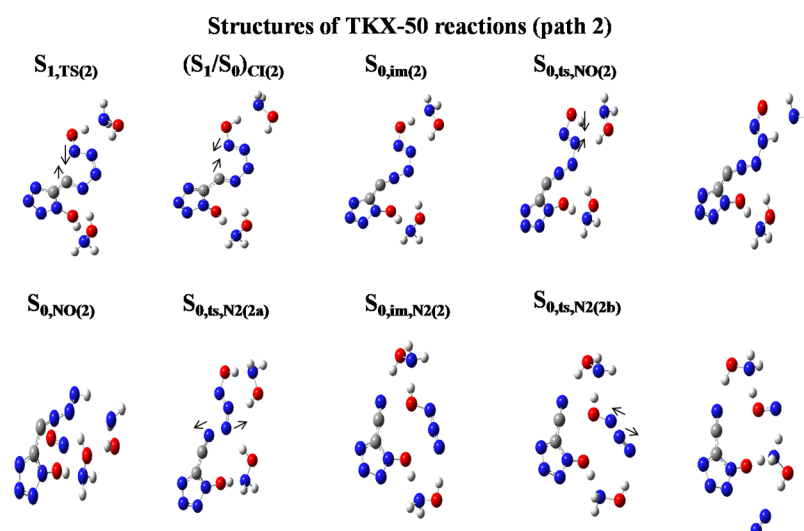


**Figure 11.** Structures of all critical points and conical intersections mentioned in Figure 10 for the other TKX-50 decomposition path 2. Arrows on the structures of the transition states show the reaction coordinates of the imaginary frequency. For atoms in the structure, gray is carbon, blue is nitrogen, red is oxygen, and white is hydrogen.

$S_0$ ) $_{CI(2)}$ . The adiabatic energy gap between the  $S_1$  and  $S_0$  surfaces near  $(S_1/S_0)_{CI(2)}$  is computed to be  $25 \text{ cm}^{-1}$ . The structure of  $(S_1/S_0)_{CI(2)}$  is shown in Figure 11, for which the tetrazole ring is open between C1 and N2 atoms. As the molecule evolves from  $S_1$  to  $S_0$  through  $(S_1/S_0)_{CI(2)}$ , following the IRC algorithm,<sup>53–56</sup> it passes to a stable intermediate state  $S_{0,im(2)}$ . From  $S_{0,im(2)}$ , again the molecule has two energy available reaction channels. One channel, shown in blue in Figure 10, involves a hydrogen bond with the  $\text{NH}_3\text{OH}^+$  cation: TKX-50 surmounts a 2.47 eV energy barrier to a transition state  $S_{0,ts,NO(2)}$ , moving the hydrogen bond from the amine N-oxide moiety to atom N3 to form an intermediate state  $S_{0,im,NO(2)}$ , from which the NO molecule dissociates. As the final energy of the molecule with free NO is 5.06 eV, this NO formation path is an unlikely one. The other reaction channel is shown in brown in Figure 10. The N4–N5 bond is broken, and molecule surmounts a 0.37 eV energy barrier for the concerted transition state  $S_{0,ts,N2(2a)}$  to form an intermediate state  $S_{0,im,N2(2)}$ . In the intermediate state, the  $\text{NH}_3\text{OH}$  group is dissociated from the rest of the molecule. Next, the N–N bond of the  $\text{NH}_3\text{OH}$  group is broken and, surmounting a 0.18 eV energy barrier, forms free  $\text{N}_2$ . NO is also produced in this process, but strong hydrogen bonds between the NO and the rest of the molecule exist. The vibrational energy stored in the NO product, however, can break the hydrogen bond easily to form free NO in the system. The final energy of the final molecule with free  $\text{N}_2$  and hydrogen bonded NO is  $-1.35 \text{ eV}$ . For all the reaction channels shown in Figures 8 and 10, no obvious torque is generated on the two products,  $\text{N}_2$  and NO. Therefore, both NO and  $\text{N}_2$  products should be generated with a cold rotational temperature, consistent with the experimental results.

Other potential decomposition paths, which can produce NO or  $\text{N}_2$  products, might exist. For example, NO can be released by the  $\text{NH}_3\text{OH}$  part of TKX-50, if all three N–H bonds and one O–H bond can be broken; however, this reaction path is well beyond the laser energy limit (5.5 eV) for the experimental study. As the theoretical calculation are predicated on the experimental results, such high energy reaction coordinates are not pursued for a theoretical decomposition mechanism. Hydrogen bonds can exist in the

molecule as calculated, but to obtain  $\text{N}_2$  and NO decomposition products from TKX-50 and MAD-X1, the breaking bonds must be C–N, N–O, and N–N bonds. Hydrogen bonds are too weak to affect the total decomposition reaction.

TKX-50 is electronically excited in the experiment, and the energy it absorbs contributes to its initial energy: it then decomposes initially to form  $\text{N}_2$  or NO products, following the reaction paths shown in Figures 8 and 10, on its ground electronic state potential energy surface. Thereby, the electronic excitation directly contributes to its ground state vibrational energy employed to break covalent chemical bonds. The energy difference between the laser energy, which is the original molecule energy, and the energy of the final structure with NO and/or  $\text{N}_2$  products and their internal energies is the energy released from TKX-50 decomposition in this initial molecular step. From the experimental results, the experimental vibrational temperature of the NO product is  $(2600 \pm 250) \text{ K}$ . From the NO dissociation calculation, if NO formed singly from the molecule, as in the black reaction path in Figure 8 and the blue path in Figure 10, the energy of the final molecule is above 5 eV, which is close to the laser energy limit. If the NO product is formed in these two ways, little energy will be stored in the molecule and the vibrational temperature of NO should be low. If the NO is produced after or together with the  $\text{N}_2$  product, as the purple path of Figure 8 or brown path of Figure 10, the energy of the final molecule is below 1.8 eV. Most of the energy stored in the molecule can be transferred (along the reaction coordinate) to the vibrational and translational energy of the NO product, consistent with the high experimental NO vibrational temperature. Combining both theoretical and experimental results, we conclude that most of the NO product should be created together with or after the  $\text{N}_2$  product in the reaction system: this conclusion can be verified by femtosecond laser experiments.

Moreover, the theoretical results demonstrate that the decomposition dynamics are purely nonadiabatic in nature and that conical intersections can lead rapidly and efficiently to internal conversion from upper to lower electronic states through these nonadiabatic radiationless transitions. During this internal conversion, electronic energy in the upper state is

converted to vibrational energy in the lower state with a potential time scale of a few tens of femtoseconds. The molecule returns to the ground electronic potential surface far from the original FC equilibrium position and can thereby undergo very different unimolecular chemistry than anticipated for its  $S_0$  FC structure. Conical intersections are now firmly established to be the key features in the excited electronic state chemistry of organic molecules in general and energetic molecules (and salts) in particular. Energized molecules move from highly excited electronic states to the ground state via conical intersections and decompose on the ground state surface releasing energy from the internal vibrational degrees of freedom: this is why product NO has a high vibrational temperature and why conical intersections are a significant and essential component of any proposed reaction mechanism. Transition states for the formation of NO and/or  $N_2$  have to be located as well to verify that the given product rotational temperatures are also low. These unique and coupled products along with their dynamical features are the main qualitative issues addressed by both experiments and supporting theory.

**B. Theoretical Calculations for MAD-X1.** A schematic one-dimensional projection of the multidimensional singlet potential energy surfaces ( $S_0$  and  $S_1$ ) of the MAD-X1 dianion, with locations and potential energies (the presented energies are not corrected for zero-point energy) for different critical points and conical intersections along the minimum energy reaction path, is plotted in Figure 12. Arrows in Figure 12 indicate different possible decomposition channels for the MAD-X1 dianion. Structures for each critical point and conical intersection are summarized in Figure 13. As depicted in Figure 12, the MAD-X1 dianion is excited to its first excited electronic state  $S_1$  (226–283 nm) and then moves rapidly to the stable structure  $S_{1,\min}$ , which is the point with minimum energy on the  $S_1$  surface. Then the MAD-X1 dianion surmounts either a 2.10 eV energy barrier for transition state  $S_{1,TS,NO}$  or a 1.86 eV energy barrier for transition state  $S_{1,TS,N_2}$ , and undergoes a rapid nonadiabatic, internal conversion from  $S_1$  to  $S_0$  state through the  $(S_1/S_0)_{CI}$  conical intersections. There are two conical intersections in Figure 12 related to the two transition states on the  $S_1$  surface leading to different reaction channels: at  $(S_1/S_0)_{CI,N_2}$ , the oxygen atom is transferred from the amine N-oxide to the C1 atom; and at  $(S_1/S_0)_{CI,NO}$ ,  $NO_2$  leaves the triazole ring to form nitro–nitrite isomerization species. The adiabatic energy gap between the  $S_1$  and  $S_0$  surfaces near  $(S_1/S_0)_{CI,N_2}$  and  $(S_1/S_0)_{CI,NO}$  are computed to be 16 and  $344\text{ cm}^{-1}$ , respectively. If the molecule goes through conical intersection  $(S_1/S_0)_{CI,N_2}$  to the  $S_0$  surface, the triazole ring will open easily and the  $N_2$  product will be dissociated as shown in red in Figure 12. In moving back to the Franck–Condon structure from  $(S_1/S_0)_{CI,N_2}$ , the molecule must surmount a 1.24 eV energy for the transition states  $S_{0,TS,N_2}$ , which makes the reaction path less favorable. No energy barrier exists between  $(S_1/S_0)_{CI,N_2}$  and the molecule with a free  $N_2$  product,  $S_{0,N_2}$ . If MAD-X1 goes through the other conical intersection  $(S_1/S_0)_{CI,NO}$ , as shown in green in Figure 12, the MAD-X1 dianion undergoes a nitro–nitrite isomerization  $S_{1,nitrite}$  based on the IRC algorithm, and then it surmounts an energy barrier of 3.17 eV on the  $S_0$  state surface with respect to  $S_{0,nitrite}$  as NO departs the molecule. During the  $N_2$  and NO dissociation processes, no obvious torque on the departing diatomics is observed in the calculation acting on the  $N_2$  or NO product: the  $N_2$  and NO products should, thereby, have cold rotational temperatures. In sum, under all four excitation conditions, MAD-X1 can decompose

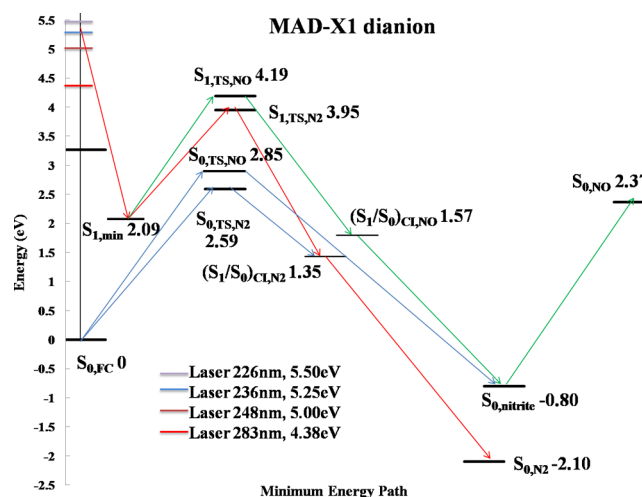


**Figure 12.** Schematic one-dimensional projection of the multidimensional energy surfaces for MAD-X1 dianion dissociation path computed at the CASSCF(8,8)/6-31G(d) level of theory. The red and green arrows represent different reaction channels for  $N_2$  and NO dissociation and the blue arrows represent the reaction path on the ground electronic state.  $S_{0,FC}$  is the optimized minimum energy of MAD-X1 dianion on the  $S_0$  state.  $(S_1/S_0)_{CI,NO}$  and  $(S_1/S_0)_{CI,N_2}$  are the conical intersections between the  $S_0$  and  $S_1$  states.  $(S_1/S_0)_{CI,NO}$  is related to a nitro–nitrite structure for NO formation, and  $(S_1/S_0)_{CI,N_2}$  is related to the transfer of an oxygen atom for  $N_2$  production.  $S_{1,TS,NO}$  and  $S_{1,TS,N_2}$  are the excited transition states on the  $S_1$  surface between the minimum structure on the  $S_{1,\min}$  and the conical intersections  $(S_1/S_0)_{CI,NO}$  and  $(S_1/S_0)_{CI,N_2}$ , respectively.  $S_{0,nitrite}$  is the intermediate state on  $S_0$  after  $(S_1/S_0)_{CI,NO}$ .  $S_{0,TS,NO}$  and  $S_{0,TS,N_2}$  are the transition states on the  $S_0$  surface between  $S_{0,FC}$  and conical intersections  $(S_1/S_0)_{CI,NO}$  and  $(S_1/S_0)_{CI,N_2}$ , respectively. As molecules pass the conical intersections, they will not return to the ground state Franck–Condon structure, but will follow the reaction coordinate to form NO and  $N_2$ :  $S_{0,NO}$  is the NO dissociated product on the  $S_0$  state, and  $S_{0,N_2}$  is the  $N_2$  dissociated product on the  $S_0$  state.

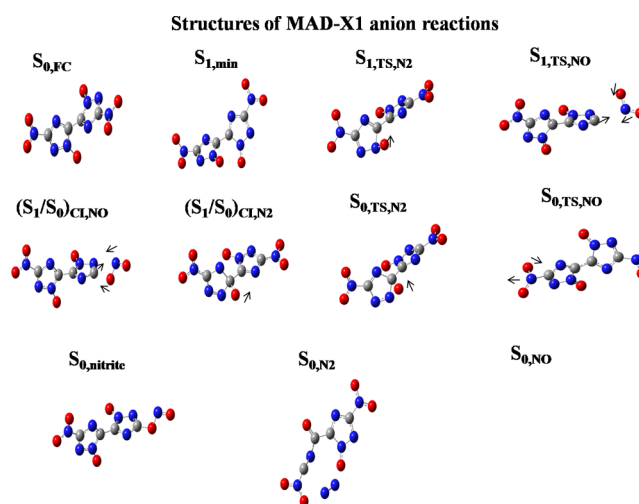


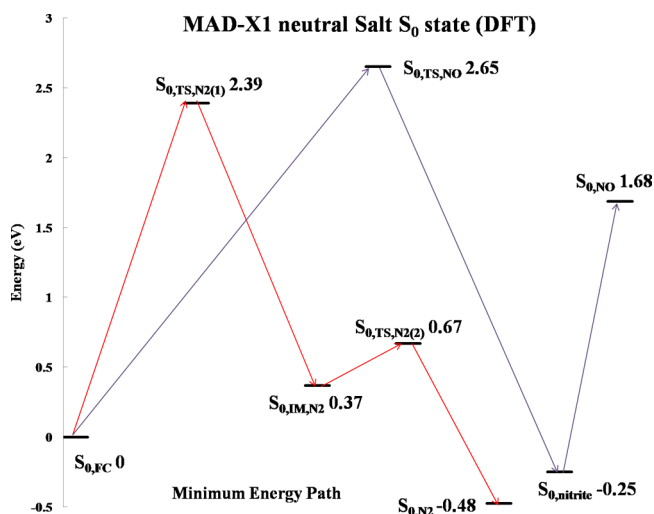
**Figure 13.** Structures of all critical points and conical intersections mentioned in Figure 12 for the MAD-X1 dianion decomposition. Arrows on the structures of the transition states show the reaction coordinates of the imaginary frequency. For atoms in the structure, gray is carbon, blue is nitrogen, and red is oxygen.

to  $N_2$  and NO products with cold rotational temperatures. Unlike the situation found for TKX-50, for which  $N_2$  and NO products are produced from two different related reaction

mechanisms, for MAD-X1, the calculated reaction mechanism does not readily reveal which product leaves the ionic system first.

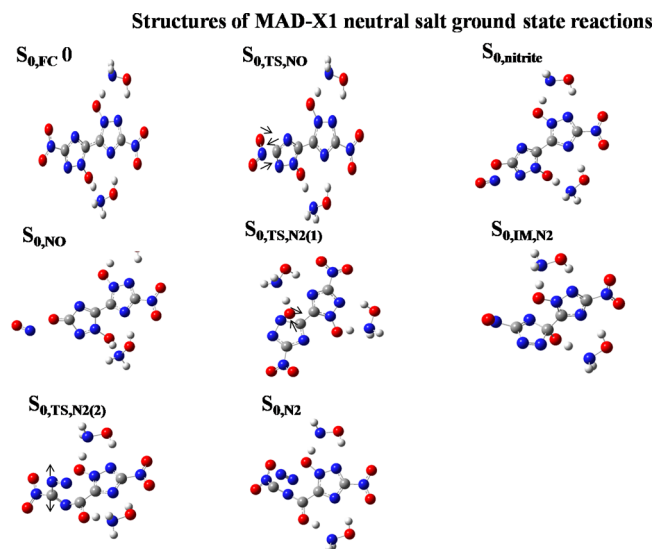
The experimental vibrational temperature of the NO product from MAD-X1 is 1500 K. In the NO dissociation calculation, similar to what has been found previously for energetic materials, NO is formed through a nitro–nitrite isomerization. The molecular decomposition occurs on the  $S_0$  state, and most of the energy stored in the molecule is transferred to the vibrational and translational energy of the NO product. Compared to TKX-50, the experimental vibrational temperature of the NO product for MAD-X1 is about 1000 K lower than that for NO from TKX-50. Two possible reasons for this difference are as follows. First, NO is produced by two different mechanisms: for TKX-50 NO is released from the amine N-oxide part of the molecule by a ring opening process, while for MAD-X1 NO is produced from nitro–nitrite isomerization. Second, energy of the TKX-50 molecule with free NO and  $N_2$  products is 1.78 eV, while the MAD-X1 molecule with a free NO product has an energy of 2.37 eV, which in this case implies more energy can be stored in and/or transferred to vibration of the NO product for TKX-50.

Figure 14 presents the schematic, one-dimensional projection of the multidimensional singlet ground potential energy surface



**Figure 14.** Schematic one-dimensional projection of the multidimensional energy surface for the MAD-X1 neutral salt ground state dissociation path computed at the DFT (B3LYP/6-31g(d)) level of theory. The red and purple arrows represent different reaction channels for  $N_2$  and NO dissociation, respectively.  $S_{0,FC}$  is the optimized minimum energy of MAD-X1 salt on the  $S_0$  state.  $S_{0,TS,NO}$ ,  $S_{0,TS,N2(1)}$ , and  $S_{0,TS,N2(2)}$  are the transition states on the  $S_0$  surface along the NO and  $N_2$  formation channels.  $S_{0,nitrite}$  and  $S_{0,IM,N2}$  are the intermediate states on  $S_0$ , while  $S_{0,NO}$  is NO dissociated products on the  $S_0$  state, and  $S_{0,N2}$  is  $N_2$  decomposition products on the  $S_0$  state.

$S_0$  of MAD-X1 neutral salt with locations and potential energies (the presented energies are not corrected for zero-point energy) for different critical points and conical intersections along the minimum energy reaction path, as calculated by the DFT algorithm. Arrows in Figure 14 indicate different possible decomposition channels for MAD-X1. Structures for each critical point and conical intersection are summarized in Figure 15. The MAD-X1 salt should surmount an energy barrier of 2.39 or 2.65 eV, respectively, to obtain  $N_2$  or NO products, while for the MAD-X1 dianion these two energy barriers are



**Figure 15.** Structures of all critical points and conical intersections mentioned in Figure 14 for the MAD-X1 neutral salt ground state decomposition. Arrows on the structures of the transition states show the reaction coordinates of the imaginary frequency. For atoms in the structure, gray is carbon, blue is nitrogen, red is oxygen, and white is hydrogen.

2.59 and 2.85 eV as shown from the blue paths in Figure 11: these latter values are quite close to those of the salt. The structure of the intermediate state  $S_{0,IM,N2}$  in Figure 13 for the MAD-X1 salt on the  $N_2$  formation path is close to the conical intersection  $(S_1/S_0)_{CI,N2}$  structure in Figure 11 for the MAD-X1 dianion, in which an oxygen atom is transferred from the N-oxide moiety to the neighboring carbon atom connecting the two triazole rings. The difference between these two species is that the conical intersection  $(S_1/S_0)_{CI,N2}$  for the MAD-X1 dianion can dissociate an  $N_2$  product directly, while the intermediate state  $S_{0,IM,N2}$  for the MAD-X1 salt should pass a small energy barrier of 0.3 eV prior to  $N_2$  dissociation. Therefore, energy of the critical points in Figure 14 (MAD-X1 neutral salt, DFT) and the ground state potential energy surface in Figure 12 (MAD-X1 dianion, CASSCF) are similar as are the general potential energy topologies. Thus, the MAD-X1 dianion calculation is probably sufficient to describe the reaction properties of this energetic salt with easier and cheaper CASSCF calculations for the dianion.

From our previous studies on energetic materials and similar model nonenergetic materials, the NO product from energetic materials usually has a cold rotational temperature and a hot vibrational temperature, while from model nonenergetic species the NO product is usually rotationally hot and vibrationally cold.<sup>28–41</sup> TKX-50 behavior is consistent with the behavior of previous energetic materials reported, while the vibrational temperature of NO from MAD-X1 is about 500 K lower than other energetic materials; however, NO is not the only dissociation product from MAD-X1. An  $N_2$  product is also observed experimentally and predicted by theoretical calculation, and it may well have a high vibrational temperature following dissociation from both salt systems.

The vibrational temperature of the initial dissociation product is important in recognizing energetic molecules because initial decomposition products with high vibrational excitation are better able to propagate a chain reaction, following the initial stimulus, leading to detonation. Energetic

molecules have an efficient single pathway to release their entire chemically stored energy during the excited electronic state decomposition process. With hot vibrational  $N_2$  and NO as initial dissociation products, the energetic properties of both TKX-50 and MAD-X1 are similar or even better than the older energetic materials. The  $S_n \rightarrow \dots \rightarrow S_0$  pathway through a series of conical intersections leaves the molecule on a new part of the  $S_0$  potential energy surface, not necessarily near the FC equilibrium point.<sup>34,35</sup> Thereby, all the excitation energy is available to break internal bonds to generate reactive fragments and radicals for further reactions as maybe required to be classified as an energetic molecule.

As a final note on the calculations for both salts, the first experiment for these new energetic systems entailed a search for the spectrum of NO, as this molecule is anticipated to be the primary decomposition product following electronic excitation; as anticipated, the NO spectrum is readily observed. We then calculated the CIs for the minimum energy reaction pathway to obtain an NO molecule, but instead calculated the CI and transition states for the  $N_2$  product. After predicting the  $N_2$  reaction coordinates through a CASSCF calculation, we rearranged the experimental set up to search for the  $N_2$  spectrum and found it as reported above. Thus, the calculations in this instance preceded the experiments and thereby are sufficient, if performed without initial bias, to be predictive.

## VI. CONCLUSIONS

Decomposition of the energetic salts TKX-50 and MAD-X1 following electronic excitation has been explored via nano-second energy resolved spectroscopy. These materials create both  $N_2$  and NO as initial decomposition products under excitation energies (4.3 to 5.5 eV). The rotational temperature of NO and  $N_2$  products from both TKX-50 and MAD-X1 is cold (<30 K). The vibrational temperatures of NO product from the two energetic salts are hot (TKX-50  $2600 \pm 250$  K; MAD-X1  $1500 \pm 250$  K). On the basis of the experimental observations and CASSCF theoretical calculations, we conclude that  $N_2$  products are released by the opening of the tetrazole or triazole ring of TKX-50 and MAD-X1, respectively. NO products are released from the amine N-oxide moiety of TKX-50, and for MAD-X1, they are produced through a nitro-nitrite isomerization. NO product is released together with and/or after the formation of  $N_2$  in TKX-50, while for MAD-X1, the reaction paths for NO and  $N_2$  products are not directly related. Conical intersections are the key point for the theoretical mechanisms, as they provide nonadiabatic radiationless internal conversion between upper and lower electronic states on the femtosecond time scale and place the undissociated molecule on a new part of the ground state potential surface with all its excitation energy in the ground state vibrations available for bond breaking.

## ■ ASSOCIATED CONTENT

### Supporting Information

Calculation of TKX-50, MAD-X1, and related structures. Charge distributions of TKX-50 and MAD-X1 in crystal and gas phase. Schematic one-dimensional projection of the multidimensional energy surfaces for one of the TKX-50 dissociation paths. This material is available free of charge via the Internet at <http://pubs.acs.org>.

## ■ AUTHOR INFORMATION

### Corresponding Author

\*E-mail: [erb@lamar.colostate.edu](mailto:erb@lamar.colostate.edu).

### Notes

The authors declare no competing financial interest.

## ■ ACKNOWLEDGMENTS

This study is supported by a grant from the U.S. Army Research Office (ARO, FA9550-10-1-0454 and W911-NF13-10192) and in part by the U.S. National Science Foundation (NSF) through the XSEDE supercomputer resources provided by NCSA under Grant No. TG-CHE110083. We also want to thank Prof. Dr. Thomas M. Klapötke, Ludwig-Maximilian University of Munich for supplying the TKX-50 and MAD-X1 samples used in this study and for helpful advice on their properties and handling.

## ■ REFERENCES

- (1) Fischer, N.; Fischer, D.; Klapötke, T. M.; Piercey, D. G.; Stierstorfer, J. Pushing the Limits of Energetic Materials—the Synthesis and Characterization of Dihydroxylammonium 5,5'-Bistetrazole-1,1'-diolate. *J. Mater. Chem.* **2012**, *22*, 20418–20422.
- (2) Dippold, A. A.; Klapötke, T. M. A Study of Dinitro-bis-1,2,4-triazole-1,1'-diol and Derivatives: Design of High-Performance Insensitive Energetic Materials by the Introduction of N-oxides. *J. Am. Chem. Soc.* **2013**, *135*, 9931–9938.
- (3) Fischer, N.; Gao, L.; Klapötke, T. M.; Stierstorfer, J. Energetic Salts of 5,5'-bis(tetrazolw-2-oxide) in a Comparison to 5,5'-bis(tetrazole-1-oxide) Derivatives. *Polyhedron* **2013**, *51*, 201–210.
- (4) Bolton, O.; Simke, L. R.; Pagoria, P. F.; Matzger, A. J. High Power Explosive with Good Sensitivity: A 2:1 Crystall of CL-20: HMX. *Cryst. Growth. Des.* **2012**, *12*, 4311–4314.
- (5) Fischer, N.; Klapötke, T. M.; Reymann, M.; Stierstorfer, J. Nitrogen-Rich Salts of 1H, 1'H-5,5'-Bitetrazole-1,1'-diol: Energetic Materials with High Thermal Stability. *Eur. J. Inorg. Chem.* **2013**, *12*, 2167–2180.
- (6) Dippold, A. A.; Klapötke, T. M.; Winter, N. Insensitive Nitrogen-Rich Energetic Compounds based on the 5,5'-Dinitro-3,3'-bi-1,2,4-triazol-2-ide Anion. *Eur. J. Inorg. Chem.* **2012**, *21*, 3474–3484.
- (7) Dachs, M.; Dippold, A. A.; Gaar, J.; Holler, M.; Klapötke, T. M. A Comparative Study on Insensitive Energetic Derivatives of 5-(1,2,4-Triazol-C-yl)-tetrazoles and their 1-Hydroxy-tetrazole Analogues. *Z. Anorg. Allg. Chem.* **2013**, *639*, 2171–2180.
- (8) Zhang, Y.; Parrish, D. A.; Shreeve, J. M. Derivatives of 5-nitro-1,2,3-2H-triazole-High Performance Energetic Materials. *J. Mater. Chem. A* **2013**, *1*, 585–593.
- (9) Klapötke, T. M.; Piercey, D. G.; Stierstorfer, J. The 1,3-Diamino-1,2,3-triazolium Cations: A Highly Energetic Moiety. *Eur. J. Inorg. Chem.* **2013**, *9*, 1509–1517.
- (10) Singh, R. P.; Verma, R. D.; Meshri, D. T.; Shreeve, J. M. Energetic Nitrogen-Rich Salts and Ionic Liquids. *Angew. Chem., Int. Ed.* **2006**, *45*, 3584–3601.
- (11) Thottempudi, V.; Forohor, F.; Parrish, D. A.; Shreeve, J. M. Tris(triazolo)benzene and Its Derivatives: High-Density Energetic Materials. *Angew. Chem., Int. Ed.* **2012**, *51*, 9881–9885.
- (12) Dippold, A. A.; Klapötke, T. M. Nitrogen-Rich Bis-1,2,4-triazoles—A Comparative Study of Structural and Energetic Properties. *Chem.—Eur. J.* **2012**, *18*, 16742–16753.
- (13) Klapötke, T. M.; Piercey, D. G. 1,1'-Azobis(tetrazole): A highly Energetic Nitrogen-Rich Compound with a  $N_{10}$  Chain. *Inorg. Chem.* **2011**, *50*, 2732–2734.
- (14) Klapötke, T. M.; Piercey, D. G.; Stierstorfer, J. The Taming of  $CN_7^-$ : The Azidotetrazolate 2-Oxide Anion. *Chem.—Eur. J.* **2011**, *17*, 13068–13077.
- (15) Fischer, N.; Klapötke, T. M.; Marchner, S.; Rusan, M.; Scheutzwow, S.; Stierstorfer, J. A Selection of Alkali and Alkaline

Earth Metal Salts of 5,5'-Bis(1-hydroxytetrazole) in Pyrotechnic Compositions. *Propellants Explos. Pyrotech.* **2013**, *38*, 448–459.

(16) Pagoria, P. F.; Lee, G. S.; Mitchell, A. R.; Schmidt, R. D. A Review of Energetic Materials Synthesis. *Thermochim. Acta* **2002**, *384*, 187–204.

(17) Fischer, N.; Izsak, D.; Klapötke, T. M.; Stierstorfer, J. The Chemistry of 5-(Tetrazol-1-yl)-2H-tetrazole: An Explosive Study of Structural and Energetic Properties. *Chem.—Eur. J.* **2013**, *19*, 8948–8957.

(18) Dippold, A. A.; Izsak, D.; Klapötke, T. M. A Study of 5-(1,2,4-Triazol-C-yl)tetrazol-1-ols: Combining the Benefits of Different Heterocycles for the Design of Energetic Materials. *Chem.—Eur. J.* **2013**, *19*, 12042–12051.

(19) Singh, H.; Mukherjee, U.; Saini, R. S. Computational Studies on Nitro Derivatives of 1-Hydroxy-1,2,4-triazole. *J. Energy Mater.* **2012**, *30*, 265–281.

(20) Wang, K.; Parrish, D. A.; Shreeve, J. M. 3-Azido-N-nitro-1H-1,2,4-triazol-5-amine-Based Energetic Salts. *Chem.—Eur. J.* **2011**, *17*, 14485–14492.

(21) Izsak, D.; Klapötke, T. M.; Reuter, S. Salts of 5-(5-Azido-1H-1,2,4-triazol-3-yl)tetrazol-1-ol: From Highly Sensitive Primary Explosives to Insensitive Nitrogen-Rich Salts. *Eur. J. Inorg. Chem.* **2013**, *32*, 5641–5651.

(22) Greenfield, M.; Guo, G. Q.; Bernstein, E. R. Ultrafast Photodissociation Dynamics of HMX/RDX From the Excited Electronic States Via Femtosecond Laser Pump-Probe Techniques. *Chem. Phys. Lett.* **2006**, *430*, 277–281.

(23) Adams, G. F. Chemical Reactions in Energetic Materials. *Annu. Rev. Phys. Chem.* **1992**, *43*, 311–340.

(24) Oyumi, Y.; Brill, T. B. Thermal Decomposition of Energetic Materials 3. A High-rate, in situ, FTIR Study of the Thermolysis of RDX and HMX with Pressure and Heating Rate as Variables. *Combust. Flame* **1985**, *62*, 213–224.

(25) Gobel, M.; Karaghiosoff, K.; Klapötke, T. M.; Piercey, D. G.; Stierstorfer, J. Nitrotetrazolate-2N-oxides and the Strategy of N-Oxide Introduction. *J. Am. Chem. Soc.* **2010**, *132*, 17216–17226.

(26) Molchanova, M. S.; Pivina, T. S.; Arnautova, E. A.; Zefirov, N. S. Computer-Aided Search for High-density Energetic Compounds among Hydrogen-free Heterocycles. *J. Mol. Struct.* **1999**, *465*, 11–24.

(27) An, Q.; Liu, W.-G.; Goddard, W. A., III; Cheng, T.; Zybin, S. V.; Xiao, H. Initial Steps of Thermal Decomposition of Dihydroxylammonium 5,5'-bistetrazole-1,1'-diolate crystals from Quantum Mechanics. *J. Phys. Chem. C* **2014**, *118*, 27175–27181.

(28) Bhattacharya, A.; Guo, Y. Q.; Bernstein, E. R. Nonadiabatic Reactions of Energetic Molecules. *Acc. Chem. Res.* **2010**, *43*, 1476–1485.

(29) Guo, Y. Q.; Bhattacharya, A.; Bernstein, E. R. Decomposition of Nitramine Energetic Materials in Excited Electronic States: RDX and HMX. *J. Chem. Phys.* **2005**, *122*, 244310–244316.

(30) Guo, Y. Q.; Greenfield, M.; Bhattacharya, A.; Bernstein, E. R. On the Excited Electronic State Dissociation of Nitramine Energetic Materials and Model Systems. *J. Chem. Phys.* **2007**, *127*, 154301–154311.

(31) Bhattacharya, A.; Guo, Y. Q.; Bernstein, E. R. Unimolecular Decomposition of Tetrazine-N-oxide Based High Nitrogen Content Energetic Materials from Excited Electronic States. *J. Chem. Phys.* **2009**, *131*, 194304–134312.

(32) Bhattacharya, A.; Guo, Y. Q.; Bernstein, E. R. Experimental and Theoretical Exploration of the Initial Steps in the Decomposition of a Model Nitramine Energetic Material: Dimethylnitramine. *J. Phys. Chem. A* **2009**, *113*, 811–823.

(33) Yu, Z.; Bernstein, E. R. Decomposition of Pentaerythritoltrinitrate [C(CH<sub>2</sub>ONO<sub>2</sub>)<sub>4</sub>] Following Electronic Excitation. *J. Chem. Phys.* **2011**, *135*, 154305–154315.

(34) Yu, Z.; Bernstein, E. R. Experimental and Theoretical Studies of the Decomposition of New Imidazole Based Energetic Materials: Model systems. *J. Chem. Phys.* **2012**, *137*, 114303–114314.

(35) Yu, Z.; Bernstein, E. R. On the Decomposition Mechanisms of New Imidazole-Based Energetic Materials. *J. Phys. Chem. A* **2013**, *117*, 1756–1764.

(36) Guo, Y. Q.; Bhattacharya, A.; Bernstein, E. R. Decomposition of Excited Electronic State s-Tetrazine and Its Energetic Derivatives. *J. Chem. Phys.* **2011**, *134*, 024318–024326.

(37) Guo, Y. Q.; Bhattacharya, A.; Bernstein, E. R. Excited Electronic State Decomposition of Furazan Based Energetic Materials: 3,3'-Diamino-4,4'-azoxyfurazan and Its Model Systems, Diaminofurazan and Furazan. *J. Chem. Phys.* **2008**, *128*, 034303–034314.

(38) Bhattacharya, A.; Bernstein, E. R. Nonadiabatic Decomposition of Gas-Phase RDX through Conical Intersections: An ONIOM-CASSCF Study. *J. Phys. Chem. A* **2011**, *115*, 4135–4147.

(39) Guo, Y. Q.; Bhattacharya, A.; Bernstein, E. R. Ultrafast S<sub>1</sub> to S<sub>0</sub> Internal Conversion Dynamics for Dimethylnitramine through a Conical Intersection. *J. Phys. Chem. A* **2011**, *115*, 9349–9353.

(40) Yuan, B.; Yu, Z.; Bernstein, E. R. Azole Energetic Materials: Initial Mechanisms for the Energy Release from Electronically Excited Nitropryrazoles. *J. Chem. Phys.* **2014**, *140*, 034320–034331.

(41) Yuan, B.; Yu, Z.; Bernstein, E. R. Initial Decomposition Mechanism for the Energy Release from Electronically Excited Energetic Materials: FOX-7 (1,1-diamino-2,2-dinitroethene, C<sub>2</sub>H<sub>4</sub>N<sub>4</sub>O<sub>4</sub>). *J. Chem. Phys.* **2014**, *140*, 074708–074717.

(42) Furman, D.; Kosloff, R.; Dubnikova, F.; Zybin, S. V.; Goddard, W. A., III; Rom, N.; Hirshberg, B.; Zeiri, Y. Decomposition of Condensed Phase Energetic Materials: Interplay between Uni- and Bimolecular Mechanisms. *J. Am. Chem. Soc.* **2014**, *136*, 4192–4200.

(43) Tsyshkevsky, R. V.; Sharia, O.; Kuklja, M. M. Thermal Decomposition Mechanisms of Nitroesters: Ab Initio Modeling of Pentaerythritol Tetranitrate. *J. Phys. Chem. C* **2013**, *117*, 18144–18153.

(44) Tsyshkevsky, R. V.; Kuklja, M. M. Decomposition Mechanisms and Kinetics of Novel Energetic Molecules BNFF-1 and ANFF-1: Quantum-Chemical Modeling. *Molecules* **2013**, *18*, 8500–8517.

(45) Kuklja, M. M. Role of Electronic Excitations in Explosive Decomposition of Solids. *J. Appl. Phys.* **2001**, *89*, 4156–4166.

(46) Reed, E. J.; Joannopoulos, J. D.; Fried, L. E. Electronic Excitations in Shocked Nitromethane. *Phys. Rev. B* **2000**, *62*, 16500–16509.

(47) Larina, L.; Lopyrev, L. *Nitroazoles: Synthesis, Structure and Applications*; Springer: New York, 2009.

(48) Im, H.-S.; Bernstein, E. R. On the Initial Steps in the Decomposition of Energetic Materials from Excited Electronic States. *J. Chem. Phys.* **2000**, *113*, 7911–7918.

(49) Im, H.-S.; Bernstein, E. R. Photodissociation of NO<sub>2</sub> in the Region 217–237 nm: Nascent NO Energy Distribution and Mechanism. *J. Phys. Chem. A* **2002**, *106*, 7565–7572.

(50) Carleton, K. L.; Welge, K. H.; Leone, S. R. Detection of Nitrogen Rotational Distributions by Resonant 2 + 2 Multiphoton Ionization Through The a<sup>1</sup>Π<sub>g</sub> State. *Chem. Phys. Lett.* **1985**, *115*, 492–495.

(51) Sitz, G. O.; Kummel, A. C.; Zare, R. N. Population and Alignment of N<sub>2</sub> Scattered from Ag(111). *J. Vac. Sci. Technol. A* **1987**, *5*, 513–517.

(52) Aoz, F. J.; Banares, L.; Herrero, V. J.; Martinez-Haya, B.; Menendez, M.; Quintana, P.; Tanarro, L.; Verdasco, E. Low-Temperature Rotational Relaxation of N<sub>2</sub> in Collisions with Ne. *J. Phys. Chem. A* **2011**, *105*, 6976–6982.

(53) Ishida, K.; Morokuma, K.; Komornicki, A. The Intrinsic Reaction Coordinate. An ab Initio Calculation for HNC<sup>+</sup>+HCN and H<sup>+</sup>+CH<sub>4</sub><sup>+</sup>+CH<sub>4</sub>+H<sup>-</sup>. *J. Chem. Phys.* **1977**, *66*, 2153–2156.

(54) Gonzalez, C.; Schlegel, H. B. An Improved Algorithm for Reaction Path Following. *J. Chem. Phys.* **1989**, *90*, 2154–2161.

(55) Taketsugu, T.; Gordon, M. S. Dynamic Reaction Path Analysis Based on an Intrinsic Reaction Coordinate. *J. Chem. Phys.* **1995**, *103*, 10042–10049.

(56) Yoshizawa, K.; Shiota, Y.; Yamabe, T. Intrinsic Reaction Coordinate Analysis of the Conversion of Methane to Methanol by an

Iron-oxo Species: A Study of Crossing Seams of Potential Energy Surfaces. *J. Chem. Phys.* **1999**, *111*, 538–545.

(57) Simpson, C. J. S. M.; Griffiths, P. T.; Wallaart, H. L.; Towrie, M. Photodissociation of Alkyl Nitrites Adsorbed on an  $\text{MgF}_2$  Surface. Rotational and Translational Energy Distributions of Product  $\text{NO}(\nu, j)$  Molecules. *Chem. Phys. Lett.* **1996**, *263*, 19–24.

(58) Mori, H.; Ishida, T.; Aoki, Y.; Niimi, T. Spectroscopic Study of REMPI for Rotational Temperature Measurement in Highly Rarefied Gas. *AIP Conf. Proc.* **2001**, *585*, 956–963.

(59) Roos, B. O.; Andersson, K.; Fulscher, M. P. Towards an Accurate Molecular Orbital Theory for Excited States: the Benzene molecule. *Chem. Phys. Lett.* **1992**, *192*, 5–13.

(60) Streit, L.; Machado, F. B. C.; Custodio, R. Double Ionization Energies of HCl, HBr,  $\text{Cl}_2$  and  $\text{Br}_2$  Molecules: An MRCI study. *Chem. Phys. Lett.* **2011**, *506*, 22–25.